NUMERICAL INVESTIGATION OF STIRRED TANK HYDRODYNAMICS

A THESIS SUBMITTED TO
THE GRADUATE SCHOOL OF NATURAL AND APPLIED SCIENCES
OF
THE MIDDLE EAST TECHNICAL UNIVERSITY

BY

KERİM YAPICI

IN PARTIAL FULFILLMENT OF THE REQUIREMENTS FOR THE DEGREE
OF MASTER OF SCIENCE
IN
THE DEPARTMENT OF CHEMICAL ENGINEERING

SEPTEMBER, 2003

Approval of the Graduate School of Natural and Applied Sciences

Prof. Dr. Canan ÖZGEN
Director

I certify that this thesis satisfies all the requirements as a thesis for the degree of Master of Science.

Prof. Dr. Timur DOĞU
Head of Department

This is to certify that we have read this thesis and that in our opinion it is fully adequate, in scope and quality, as a thesis and for the degree of Master of Science.

Assist.Prof. Dr. Yusuf ULUDAĞ
Supervisor

Examining Committee Members

Prof. Dr. Levent YILMAZ (Chairman) _____

Assoc. Prof. Dr. İsmail AYDIN _____

Assoc. Prof. Dr. Gürkan KARAKAŞ _____

Assist. Prof. Dr. Halil KALIPÇILAR _____

Assist. Prof. Dr. Yusuf ULUDAĞ _____

ABSTRACT

NUMERICAL INVESTIGATION OF STIRRED TANK HYDRODYNAMICS

Yapıcı, Kerim
M.Sc., Department of Chemical engineering
Supervisor: Ass.Prof.Dr. Yusuf Uludağ

September 20003, 93 pages

A theoretical study on the hydrodynamics of mixing processes in stirred tanks is described. The primary objective of this study is to investigate flow field and power consumption generated by the six blades Rushton turbine impeller in baffled, flat-bottom cylindrical tank both at laminar and turbulent flow regime both qualitatively and quantitatively. Experimental techniques are expensive and time consuming in characterizing mixing processes. For these reasons, computational fluid dynamics (CFD) has been considered as an alternative method. In this study, the velocity field and power requirement are obtained using FASTEST, which is a CFD package. It employs a fully conservative second order finite volume method for the solution of Navier-Stokes equations. The inherently time-dependent geometry of stirred vessel is simulated by a multiple frame of reference approach.

The flow field obtained numerically agrees well with those published experimental measurements. It is shown that Rushton turbine impeller creates predominantly radial jet flow pattern and produces two main recirculation flows one above and the other below the impeller plane. Throughout the tank impeller plane dimensionless radial velocity is not affected significantly by the increasing impeller

speed and almost decreases linearly with increase in radial distance. Effect of the baffling on the radial and tangential velocities is also investigated. It is seen that tangential velocity is larger than radial velocity at the same radial position in unbaffled system.

An overall impeller performance characteristic like power number is also found to be in agreement with the published experimental data. Also power number is mainly affected by the baffle length and increase with increase in baffle length. It is concluded that multiple frame of reference approach is suitable for the prediction of flow pattern and power number in stirred tank.

Keywords: Stirred Tank, Mixing, Rushton Turbine, Computational Fluid Dynamics (CFD), Multiple Frame of Reference

ÖZ

KARIŞTIRMA TANKI HİDRODİNAMİĞİNİN NÜMERİK İNCELENMESİ

Yapıcı, Kerim
Yüksek Lisans, Kimya Mühendisliği Bölümü
Danışmanı: Y.Doç.Dr. Yusuf Uludağ

Eylül 2003, 93 sayfa

Karıştırmalı tanklarda karıştırma sürecinin hidrodinamiği üzerine teorik bir çalışma yapılmıştır. Çalışmanın temel amacı hem laminer hem de türbülent akış rejimlerinde kırıcı yerleştirilmiş düz tabanlı silindirik tankta altı kanatçıklı Rushton tip karıştırıcı ile oluşturulan akış profili ve güç harcamasının nitel ve nicel incelenmesidir. Akış süreçlerinin karakterize edilmesinde kullanılan deneysel teknikler hem fazla zaman gerektirir hem de pahalıdır. Bu sebeplerden dolayı, hesaplamalı akışkan dinamiği alternatif bir metod olarak görülebilir. Bu çalışmada akış profili ve güç harcamaları bir paket program olan FASTEST kullanılarak elde edilmiştir. Bu program da Navier-Stokes eşitliklerinin çözümü için tam korunumlu ikinci dereceden sonlu hacimler metodu kullanılmaktadır. Karıştırmalı tankın kaçınılmaz olarak zamana bağlı geometrisinin simülasyonu, çoklu referans düzlemi yaklaşımı ile yapılmıştır.

Bu çalışmada sayısal yötemlerle bulunan akış alanı literatürdeki deneysel sonuçlarla uyum içerisindedir. Rushton tip karıştırıcının ağırlıklı olarak radyal jet-akışı ve birisi karıştırıcı düzleminin üzerinde diğeride altında olmak üzere iki ana

akışkan dolanımı oluşturduğu görülmüştür. Tank boyunca karıştırıcı düzlemindeki normalize edilmiş radyal yöndeki hızın artan karıştırıcı hızından önemli ölçüde etkilenmediği ve artan radyal yönle nerdeyse doğrusal olarak azaldığı bulunmuştur. Kırıcının radyal ve açısal hızlar üzerindeki etkisi ayrıca incelenmiştir. Kırıcı kullanılmayan sistemde aynı radyal pozisyonda açısal hızın radyal hızdan daha büyük olduğu görülmüştür.

Bir karıştırıcı performans özelliği olan güç sayısının yayınlanmış deneysel sonuçlarla uyum içinde olduğu bulunmuştur. Ayrıca güç sayısının ağırlıklı olarak kırıcı genişliğinden etkilendiği ve artan kırıcı genişliği ile arttığı bulunmuştur.

Sonuç olarak, çoklu referans düzlemi karıştırmalı tanklarda akış özellikleri ve güç sayısının tahmini için uygun bir yaklaşımdır.

Anahtar Kelimeler: Karıştırmalı Tank, Karıştırma, Rushton Karıştırıcı, Hesaplamalı Akışkan Dinamiği, Çoklu Referans Düzlemi

to my family

ACKNOWLEDGEMENTS

First of all I would like to thank my supervisor Ass.Prof.Dr. Yusuf Uludağ for his continual advice and suggestions, and his trust in me. I express sincere appreciation to Prof.Dr. Bülent Karasözen for his guidance and insight throught the study. I am grateful to Prof.Dr. rer.nat. M. Schafer, Senem Ertem and other staffs from Darmstad Technical University, Germany for their suggestions, comments and helps about FASTEST at the beginning of the study.

I am gratefull to my roommate Volkan Köseli for his help in the preparation of thesis report. Also I want to tank Murat Yıldırım from METU, Mathematics Department for their help in learning LINUX.

I can never fully express my gratitute for moral support of all my friends and family.

TABLE OF CONTENTS

LIST OF TABLES

TABLES

LIST OF FIGURES

FIGURES

LIST OF SYMBOLS AND ABBREVIATIONS

A: area, m^2

ADI: Alternating direction implicit

b: Impeller blade height, m

CDS: Central difference scheme

CFD: Computational fluid dynamics

D_d: Diameter of the disc, m

D_h: Diameter of the hub, m

D_i: Impeller diameter, m

D_s: Diameter of the shaft, m

D_T: Tank diameter, m

EFD: Experimental fluid dynamics

FASTEST: Flow Analysis by Solving Transport equations Simulating Turbulence

FD: Finite difference

Fr: Froude number

FV: Finite element

FV: Finite volume

g: Gravitational force, ms^{-2}

H: Height of the blade; m

H_i: Impeller height from bottom of the tank, m

H_l: Height of the liquid, m

k: turbulent kinetic energy, m^2s^{-2}

L: Length of the blade, m

LDV: Laser Doppler velocimetry

N: Impeller rotating speed, $Revs^{-1}$

N_B: Reference number for baffles

N_p: Power number

N_R: Reference number for impellers

P: Power, Watt

p: Pressure, Pa

PIV: Particle image velocimetry

q: Impeller blade with, m

R: Impeller radius, m

r: radial co-ordinate

Re: Reynold number

SIP: Strongly implicit procedure

SOR: Successive over relaxation

t: time, s

U_r: Radial velocity, ms^{-1}

U_{tip}: Impeller tip velocity, ms^{-1}

U_z: Axial velocity, ms^{-1}

U_θ: Tangential velocity, ms^{-1}

W: Length of the baffles, m

z: axial co-ordinate

Greek letters:

θ: Tangential co-ordinate
ε: Turbulent energy dissipation rate, m^2s^{-3}
μ: Viscosity, Pas
ρ: Density, kgm^{-3}
τ_{ij}: Shear stress $kgm^{-1}s^{-2}$

CHAPTER 1

INTRODUCTION

1.1 Scope

The mixing of fluids in agitated vessel is one of the most important unit operations for many industries including the chemical, bio-chemical, pharmaceutical, petrochemical, and food processing (Sahu et al., 1999). Therefore determining the level of mixing and overall behavior and performance of the mixing tanks are crucial from the product quality and process economics point of views. One of the most fundamental needs for the analysis of these processes from both a theoretical and industrial perspective is the knowledge of the flow structure in such vessels.

Depending on purpose of the operation carried out in a mixer, the best choice for the geometry of the tank and impeller type can vary widely. Different materials require different types of impellers and tank geometries in order to achieve the desired product quality. The flow field and mixing process even in a simple vessel are very complicated. The fluid around the rotating impeller blades interacts with the stationary baffles and generates a complex, three-dimensional turbulent flow. The other parameters like impeller clearance from the tank bottom, proximity of the vessel walls, baffle length also affect the generated flow. The presence of such a large number of design parameters often makes the task of optimization difficult. As a consequence, large amounts of money in the range of billions of dollars per year in

the USA (Tatterson, 1994) may be lost because of the uncertainties associated with the mixer designs.

In order to understand the fluid mechanics and develop rational design procedures there have been continuous attempts over the past century. These attempts can be broadly classified in two parts, namely experimental fluid dynamics (EFD) and computational fluid dynamics (CFD). The developments in Laser based instrumentation such as laser Doppler velocimetry (LDV), particle image velocimetry (PIV) and application of computers in experimental investigation have led to enhanced understanding of many complex fluid dynamic processes experimentally.

Experimental investigations have also contributed significantly to the better understanding of the complex hydrodynamics of stirred vessels. However such experimental studies have obvious limitations regarding the extent of parameter space that can be studied within a time frame. A wide variety of impellers with different shapes are being used in practice. The impeller clearances, impeller diameter, length, height can vary significantly for different applications. Therefore an experiment programmed to measure the discharge flows for all impellers is not economic.

Flow simulation studies for stirred vessels are generally based on steady-state analyses (Harvey and Greaves, 1982, Placek et al., 1986., Ranade et al., 1990). Most of these previous studies have treated the rotating impeller as a black box. This approach requires impeller boundary conditions as input which needs to be determined experimentally. Though this approach is successful in predicting the flow characteristics in the bulk of the vessel, its usefulness is inherently limited due to its

dependence on the availability of the experimental data. Hence it cannot be used to screen large number of alternative mixer configurations (clearance from the bottom, size and shape of the impeller blade, multiple impellers, etc.). Even with the available data, it is not at all certain that the given impeller generates the same flow leaving its periphery in all vessels. In order to overcome these drawbacks, in more recent studies the flow pattern around the impeller blades are predicted explicitly instead of using experimental data as impeller boundary conditions (Brucato et al., 1998). Explicit modeling of the impeller geometry is done through four methods. The first explicit model is momentum source method which is based on aerofoil aerodynamics (Xu and McGrath, 1996). In this model, the impeller blades are replaced with finite blade section by dividing it into a number of vertical strips from the hub to the tip. The blade section inside each strip is approximated to an aerofoil and aerofoil aerodynamics is applied. Second explicit model is sliding mesh method (Bakker et al., 1997). With the sliding mesh method, the tank is divided into two regions that are treated separately: the impeller region and the tank region that includes the bulk of the liquid, the tank wall, the tank bottom and the baffles. The grid in the impeller region rotates with the impeller while the grid in the tank remains stationary. The two grids slide past each other at a cylindrical interface.

The other model is snapshot method. This method can be explained as follows: in a real case rotation of the blade causes suction of fluid at the back side of the impeller blades and equivalent ejection of fluid from the front side of the blades. These phenomena of ejection and suction have been modeled by snapshot formulation which is discussed in more detail in Chapter 3 (Ranade and Dommeti, 1996). The last model is multiple frame of reference, which is used in this study. In

this method tank is divided into two frames. These are rotating frame and stationary frame. Rotating reference frame encompasses the impeller and the flow surrounding it and stationary frame includes the tank, the baffles and the flow outside the impeller frame (Naude et al., 1998), (Fluent, 2000).

1.2 Objective of This Study

In this study, the velocity field and power requirement are obtained using Flow Analysis by Solving Transport Equations Simulating Turbulence (FASTEST), which is a CFD package. It employs a fully conservative finite volume method for the solution of the continuity and momentum equations. In the simulations the selected mixer consists of a Rushton turbine in a baffled, flat-bottom cylindrical tank filled with silicone oil and water as working fluid. The influence of angular velocity and baffle length on the power number and generated velocity field are investigated.

CHAPTER 2

GENERAL CONSIDERATIONS IN MIXING

2.1 Mixing Phenomena

The objective of mixing is homogenization, manifesting itself in a reduction of concentration or temperature gradients or both simultaneously, within the agitated system. Quillen defines mixing as the 'intermingling of two or more dissimilar portions of a material, resulting in the attainment of a desired level of uniformity, either physical or chemical, in the final product (Holland, 1966).

Gases, confined in a container, mix rapidly by natural molecular diffusion. In liquids, however, natural diffusion is a slow process. To accelerate molecular diffusion within liquids, the mechanical energy from a rotating agitator is utilized. The rotation of an agitator in a confined liquid mass generates eddy currents. These are formed as a result of velocity gradients within the liquid. A rotating agitator produces high velocity liquid streams, which move through the vessel. When the high velocity streams come into contact with stagnant or slower mowing liquid, momentum transfer occurs. Low velocity liquid becomes entrained in faster moving streams, resulting in forced diffusion and liquid mixing.

2.2. Mixing Operations

The main applications of the mixing can be classified in terms of the following five operations:

1) Homogenization;

Homogenization can be described as the equalization of concentration and temperature differences, which is the most important and the most frequently carried out mixing operation.

2) Enhancing heat transfer between a liquid and heat transfer surface;

Mixing reduces the thickness of the liquid boundary layer hence the thermal resistance on the heat transfer surface and convective motion of the tank contents ensure that the temperature gradients within the tank content are reduced.

3) Suspension of solid in a liquid;

In continuous process homogenous distribution of the solid in the bulk of the liquid is required. By mixing the suspension, settling of the particles as a result of gravity is prevented.

4) Dispersion of two immiscible liquids;

Dispersion in liquid/liquid systems is associated with the enlargement of the interface area between two immiscible liquids. This accomplished by the lowest impeller speed at which one phase is completely mixed into the other.

5) Dispersion of a gas in a liquid.

The aim of this operation is to increase the interfacial area between the gas phase and liquid phase. Increasing the gas liquid interfacial area is obtained by gas sparging by means of stirrers.

2.3 Mixing Equipment

The classification of mixing equipment is made on both predominant flow pattern that it produces and liquid viscosity, which affects the flow created by rotating agitator. Low viscosity liquids show little resistance to flow and therefore require relatively small amounts of energy per unit volume for a condition of mixing to occur. A typical stirred vessel consists of three parts: tank, baffles and impeller. Figure 2.3.1 shows the typical tank geometry which is widely used in chemical industry.

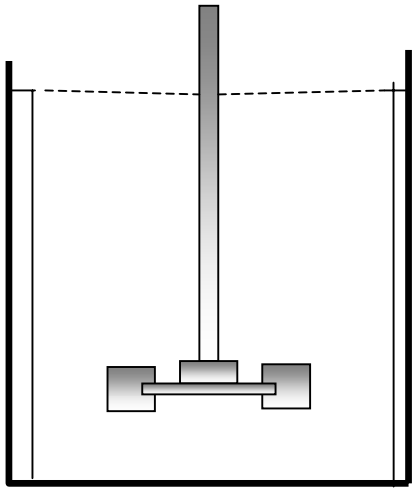

Figure 2.3.1. A typical stirred tank equipment

Tanks used in stirrer equipment can be in different shapes depending on the application. These are cylindrical vessel with a flat bottom, cylindrical vessel with a round bottom and rectangular vessels as shown Figure 2.3.2. Round bottom tanks are used mainly for solid-liquid agitation while the flat bottom tanks suit better for more viscous types of fluids.

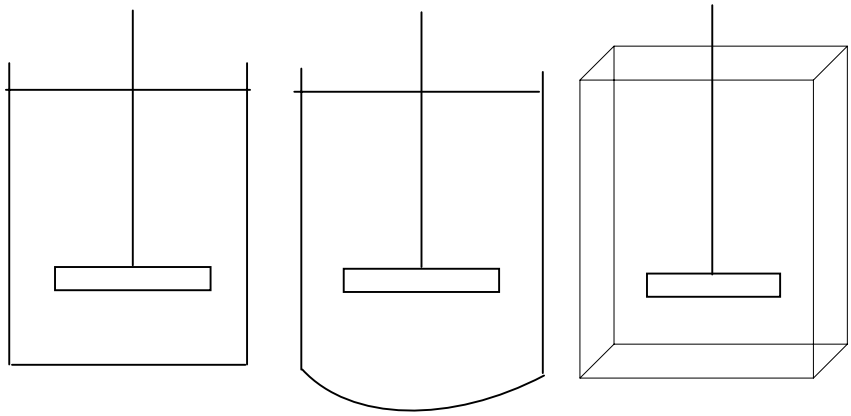

(a) (b) (c)

Figure 2.3.2. Stirred tanks (a) cylidrical with flat bottom
(b) cylindrical with round bottom (c) rectangular

Baffles are important parts of the stirred tanks which improve the mixing efficiency and suppress the vortex formation. However they increase the power requirements in the mixing tank. Several baffle arrangements are available according to their using purposes. For example they can be fixed on the tank wall or can be set away from the wall.

Impellers are the most important parts in a stirred tank. In Figure 2.3.3 the stirrer types are given according to the flow pattern that they produce as well as to the range of fluid viscosity.

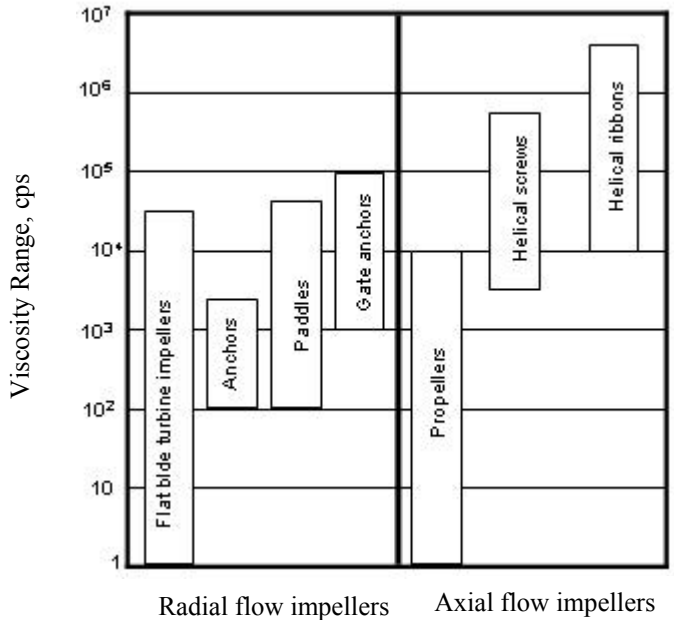

Figure 2.3.3 Classification of impeller according to the flow pattern and range of viscosity

2.3.1 Turbines and propellers

For mixing low to medium viscosity liquids, the flat blade turbine or the marine type propeller is used. One of the most common turbines is the 6 blade flat blade, disk mounted type. A common marine propeller has 3 blades, with a blade pitch equal to the propeller diameter.

A large variety of turbine agitators are available which are modifications of the flat blade design. The hub mounted curved blade turbine and disk mounted curved blade turbine are useful where the general characteristics of the flat blade type are desired but at a lower shear at the blade tip and reduced power consumption (Weber, 1964).

Another modification of the flat blade design is the pitched blade hub mounted turbine with straight blades set at less than 90^0 from the horizontal. This design provides reduced power requirements and is useful when mixing liquids with heavy solids content.

2.3.2 Helical screw impeller

The helical screw agitator is an effective device when used in high viscosity liquids (Chapman, 1962). The screw functions by carrying liquid from the vessel bottom to the liquid surface. The liquid is then discharged and returns to the tank bottom to fill the void created when fresh liquid is carried to the surface.

2.3.3 Anchor impeller

The anchor agitator is generally a slow moving, large surface area device; in close proximity to the vessel wall. It has been used in the batch mixing of liquids having high viscosity.

2.3.4 High shear impeller

High shear agitators are primarily used in liquid mixing systems where a particle size reduction or a breaking apart of agglomerated solids is required

2.4 Degree of Mixing

The degree of mixing within a system is a function of two variables: the magnitude of eddy currents or turbulence formed and the forces tending to dampen the formation of eddy currents. This relationship may be expressed:

$$\frac{\text{Driving Force}}{\text{Resistance}} = \text{Degree of mixing}$$

In this case,

Driving force= the forces producing eddy currents

Resistance= the forces tending to dampen the formation of eddy currents

A high degree of mixing occurs when the entire liquid mass, confined in a vessel, is under turbulent flow condition.

2.5 Degree of Agitation

Impeller tip speed in m/s is commonly used as a measure of the degree of agitation in a liquid mixing system. The tip speed of an agitator can be expressed:

$$TS = \pi D_i N$$

Where D_i is the diameter of the impeller in m and N is the rotational speed of the impeller in revolution per second.

2.6 Methods of Measuring Liquid Velocity

The flow characteristics of stirred vessels have been studied by many investigators using different velocity measuring devices. The first velocity measurement in a stirred vessel carried out by using the light streak method (Sachs, 1954). Improved version was used by Cutter (1966). Pitot tubes (Nagata, 1955) and hot wire anemometer (Bowers, 1965) were other types of instruments employed in the early studies on the measurements of the flow fields in mixing tanks.

None of the above devices are entirely satisfactory. Ideally a measurement device should not interface with the flow field and should permit the measurement of instantaneous velocities. Among the non-invasive and instantaneous methods, the Laser Doppler Velocimetry (LDV) in which velocity is measured using the Doppler shift of the laser beams crossing the flow field, is the most common method used in velocity measurements of the complex flows.

LDV was used by Rao and Brodkey (1972), Riet and Soots (1989), Wu and Petterson (1989), Kresta and Wood (1983). Nevertheless the flow in the stirred vessel is highly unsteady and time varying large scale motions dominate the flow. Since the LDV measures velocities on a plane, characterizing the entire flow field requires long experimental times. In addition LDV cannot be used in opaque media.

Therefore Bakker et al. (1996), Ward (1995) were the first to use Particle Image Velocimetry (PIV) to study the two dimensional flow pattern along the center plane in the vessel. PIV is quite different from the LDV methods. LDV provides instantaneous velocity field snapshot in a plane but PIV provides overall flow fields with spatially resolved eddies but with low temporal resolution.

2.7 Flow Patterns in Stirred Vessel

According to the main directions of the streamlines in the vessel, there are three principal types of flow. These are tangential flow, radial flow and axial flow.

2.7.1. Tangential flow

Tangential flow, where the liquid flows parallel to the path is shown in Figure 2.7.1.1. When the flow is predominantly tangential, discharge of liquid from the impeller to the surroundings is small. Tangential flow takes place in a paddle type impeller running at a speed, which is not sufficient to produce a noticeable action of the centrifugal force.

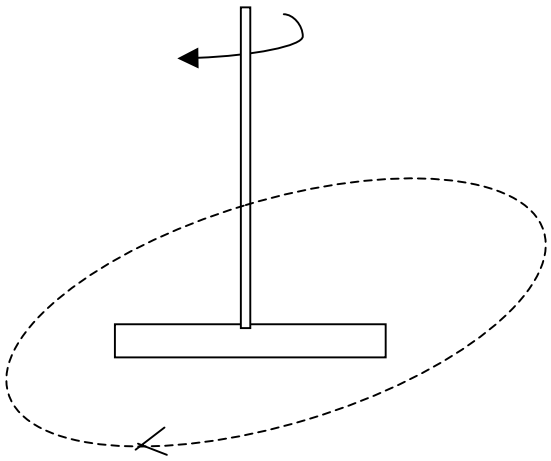

Figure 2.7.1.1. Tangential flow

2.7.2 Radial flow

The liquid discharges from the impeller at right angles to its axis and along a radius. Figure 2.7.2.1 shows the flow pattern of a impeller with its axis coinciding with that of the vessel and producing radial flow. In this case it is apparent that the impeller produces two flow sections; one is in the bottom part of the vessel it entrains the liquid in the upward direction and displaces it at right angles to the axis of the impeller; the other is in the upper part of the vessel, the impeller entrains the liquid downwards, displacing it like perpendicular to the impeller axis.

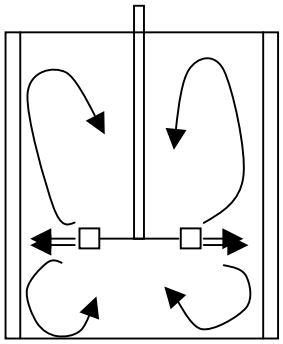

Figure 2.7.2.1 Radial flow pattern

2.7.3 Axial flow

Axial flow, in which the liquid enters the impeller and discharges from it parallel to it axis as shown in Figure 2.7.3.1.

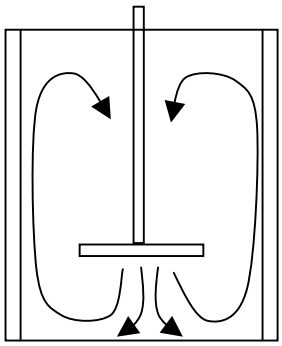

Figure 2.7.3.1. Axial flow pattern

2.8 Flow Model for The Stirred Vessel

One of the most commonly used and extensively studied impeller is the radial flow Rushton turbine. This is also chosen for this study in order to compare the results of this study with those of previous studies directly.

In baffled vessels a Rushton turbine impeller develops radial flow pattern. From the fluid dynamics view point the flow field in an agitated vessel divided into six following regions (DeSouza and Pike, 1972).

1) The flow from the impeller;

2) Impeller stream impinging on the tank wall;

3) Upper and lower corners of the tank;

4) Flow at the top and bottom of the thank axis;

5) Flow at the center of the tank axis;

6) Two doughnut shaped regions.

The most important among them is the impeller region where tank content and the impeller interacts directly and the required energy to drive the flow is transferred to the fluid. Due to the high shear rates and sudden accelerations associated with this region, capturing the flow characteristics accurately around the impeller through computational methods is a challenging task.

2.9 Power Consumption in Mixing Vessel

The velocity field in stirred vessels provides the details on how fluid moves inside the tank, no specific information of impeller performance are readily available. In fact, the power drawn by a rotating impeller is crucial for the process and mechanical design of agitated vessels.

The power consumption in a liquid mixing system is determined by its impeller rotational speed and by the various physical properties of the mixing liquid. Rushton, Costich and Everett (1950) used dimensional analysis to derive the equations

$$N_p = C(N_{\mathrm{Re}})^x (N_{Fr})^y (D_T / D_i)^a (H_l / D_i)^b (H_i / D_i)^c (q / D_i)^d (r / D_i)^e (W / D_i)^f$$

$$(B / N_B)^h (R / N_R)^i \qquad (2.9.1)$$

which, gives the dimensionless Power number N_p as a function of the Reynolds number N_{Re}, Froude number N_{Fr} and number of dimensionless shape factors. Reynold number and Froude number are defined as:

$$N_{\mathrm{Re}} = \frac{D_i^2 N \rho}{\mu}$$

$$N_{Fr} = \frac{N^2 D_i}{g}$$

where D_i is the impeller diameter (m), N is the impeller speed (s^{-1}), ρ is density (kgm^{-3}), μ is the viscosity (Pas), g is the gravitational force (ms^{-2}).

In equation (2.9.1):

C = dimensionless constant

D_i = impeller diameter

D_T = tank diameter

H_l = liquid height

H_i = impeller height from bottom of the tank

q = impeller blade with

r = impeller blade length

W = baffle length

N_B = reference number for baffles

N_R = reference number for impellers

N_B and N_R determined by convenient choice. For example, in the case of standard configuration, which is discussed in Chapter 4 is used as a reference, N_B = 4 and N_R = 6. If these shape factors remain fixed, equation 2.9.1 simplifies to

$$N_p = C(N_{\mathrm{Re}})^x (N_{Fr})^y \qquad (2.9.2)$$

where C is the over all shape factor which represents the geometry of the system. Since Froude number links gravitational forces and centrifugal inertial forces, then

fully baffled vessel in which no central vortex could form. Therefore the exponent y of the Froude number is zero, $(N_{Fr})^y$ =1 and equation 2.9.2 becomes

$$N_p = C(N_{\mathrm{Re}})^x \tag{2.9.3}$$

Power number, which is dimensionless number relating the resistance force to the inertia force is expressed as

$$N_p = \frac{P}{\rho \mathrm{N}^3 D_i^5} \tag{2.9.4}$$

where P is the power in Watt, ρ is the density in kg/m^3, N is the rotational speed of the impeller in rev/sec and D_i is the impeller diameter.

2.9.1 Power curves

A plot of N_p versus N_{Re} on log-log coordinates is commonly called a power curve. The power curve firstly was plotted by Holland and Chapman (1966) for the standard tank configuration. At low Reynolds number $(N_{\mathrm{Re}} < 10)$, Np decreases linearly with increasing Re. In this region equation (2.9.3) may be written as

$$\log_{10} N_p = \log_{10} C + x \log_{10} N_{\mathrm{Re}} \tag{2.9.5}$$

The slope x in the viscous region is equal to -1. Therefore for the viscous region, equation (2.9.5) can be simplified,

$$P = (\rho \mathrm{N}^3 D_i^5) C (\rho \mathrm{ND}_i^2 / \mu)^{-1} \tag{2.9.6}$$

which can be rearranged to

$$P = \mu(C)(N^2 D_i^3) \tag{2.9.7}$$

Equation (2.9.7) shows power to be directly proportional to viscosity at any impeller speed.

When the Reynolds number increases, flow changes from viscous to turbulent. The power and flow characteristics remain dependent only on the Reynolds number until $N_{Re} \cong 300$. At this point enough energy is being transferred to the liquid enabling vortex formation. The baffles effectively suppress vortexing and the flow remains dependent on the Reynolds number until $N_{Re} = 10000$. When flow becomes fully turbulent, the power curve becomes horizontal. Here flow is independent of both the Froude and Reynolds numbers.

.

CHAPTER 3

DISCRETIZATION METHODS IN FLUID DYNAMICS

3.1 Computational Approach

Computational fluid dynamics (CFD) is a tool for solving conservation equations for mass, momentum and energy in flow geometry of interest. Flows and associated phenomena can be described by partial differential equations, which are in many cases extremely difficult to solve analytically due to the non-linear inertial terms. To obtain accurate results the domain in which the partial differential equations are described, have to be discretized using sufficiently small grids. Therefore accuracy of numerical solution is dependent on the quality of dicretizations used (Ferziger, Peric, 1996).

3.2 Components of the Numerical Simulations

3.2.1 Mathematical model

The starting point of a numerical method is the mathematical model, which is the selection of the governing equations and initial and boundary conditions.

3.2.2 Discretization of the governing equations

After selection the governing equations, one has to choose suitable discretization method. There are many approaches, the most important are: finite difference (FD), finite volume (FV) and finite element (FE) methods. Each of these methods is used to transform differential equations to the algebraic equations.

3.2.3 Generation of computational grid

The discrete locations form numerical grid, which can also be considered as discrete representation of the solution domain. The numerical grid divides the solution domain into finite number of subdomains (elements, control volumes).

3.2.3.1 Structured grid

Structured grids consist of families of grid lines with the property that members of a single family do not cross each other and cross each member of the other families only once. This allows the lines of a given set to be numbered consecutively. The disadvantage of structured grid is that they can be used only for geometrically simple solution domains and another is that it may be difficult to obtain suitable grid distributions for complicated flow fields.

3.2.3.2 Unstructured grid

For very complex geometries, the most flexible type of grid is one, which can fit an arbitrary solution domain boundary. In principle, such grids could be used with any discretization scheme, but they are best adapted finite volume and finite element approaches. The elements or control volumes may have any shape and there is no restriction on the number of neighbor elements or nodes. Disadvantage of the unstructured system of algebraic equation is difficult to solve.

3.2.3.3 Block structured grid

In a block structured grid, there are two or more level subdivision of domain. There are blocks, which are relatively large segments of the domain; their structure may be irregular and they may or may not overlap. This kind of grid is more flexible then the structured grids, since it allows use of finer grids in regions where greater

spatial resolutions are required. The main advantage of the block structured grid is that complex geometries can be handled easily.

3.2.4 Finite approximation

After the choice of grid type, one has to select the approximations to be used in the discretization process. In the finite difference method, approximations for the derivatives at the grid points have to be selected. In the finite volume method, however, one has to select the methods of approximating surface and volume method. In the finite element method, one has to choose the functions (elements) and weight functions. The choice influences the accuracy of the approximation, also affects the difficulty of developing the solution method and speed of the code. More accurate approximations involve more nodes and result algebraic equations with dense matrices.

3.2.5 Solution method

Discretization yields a large system of non-linear algebraic equations. The method of solution depends on the problem. For example for unsteady flows, methods employed in the solution of the initial value problems are used. The solution methods of solving algebraic systems can be classified as follows:

1) Direct methods

Direct methods are based on finite number of arithmetic operations leading to the exact solution of linear algebraic system. Some of these are Gauss elimination, tridiagonal system and LU decomposition.

2) Iterative methods

Iterative methods are based on a succession of approximate solutions, leading to the exact solution after infinite number of step. A large number of iterative methods are available. Some of these are Jacobi method, Gauss-Seidel method, successive over relaxation (SOR), strongly implicit procedure (SIP) and alternating direction implicit (ADI) method.

3.2.6 Convergence criteria

Finally, one needs to set the convergence criteria for the iterative method due to decide when to stop iterative process. Usually, there are two levels of iterations, within which the linear equations are solved and outer iteration that deals with the non-linearity and coupling of the equations. Deciding when to stop the iterative process on each level is important from both the accuracy and efficiency point of views.

3.3 Finite Volume Method

Finite volume method uses the integral form of the conservation equations, which are discretized directly in the physical space. Solution domain is divided into a finite number of small control volumes (CVs) by a grid, in contrast to the finite differences (FD) method, defines the control volumes boundaries. In the finite volume method two approaches are described. In the usual approach, the solution domain is discretized and a computational node is assigned to the each control volume center. However, in the second approach nodel locations are defined first and constructed CVs around them, so that control volume is faced lie midway between nodes which boundary conditions are applied as shown in Figure 3.3.1 (J.H. Ferziger and M.Peric, 1996).

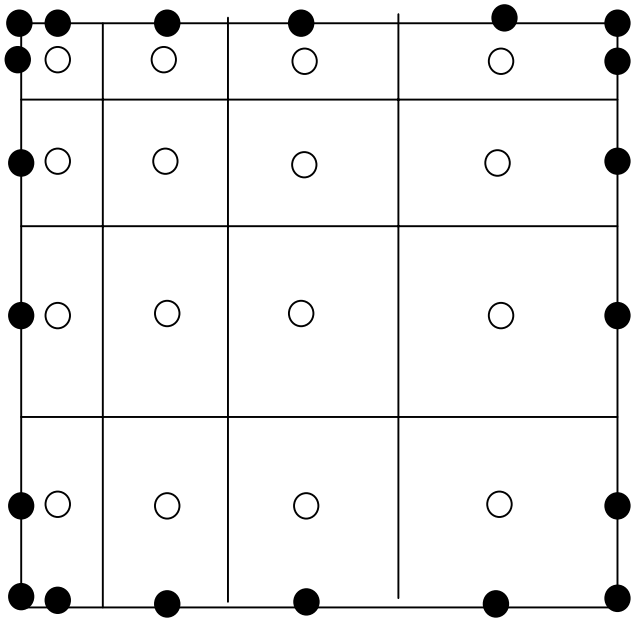

(a)

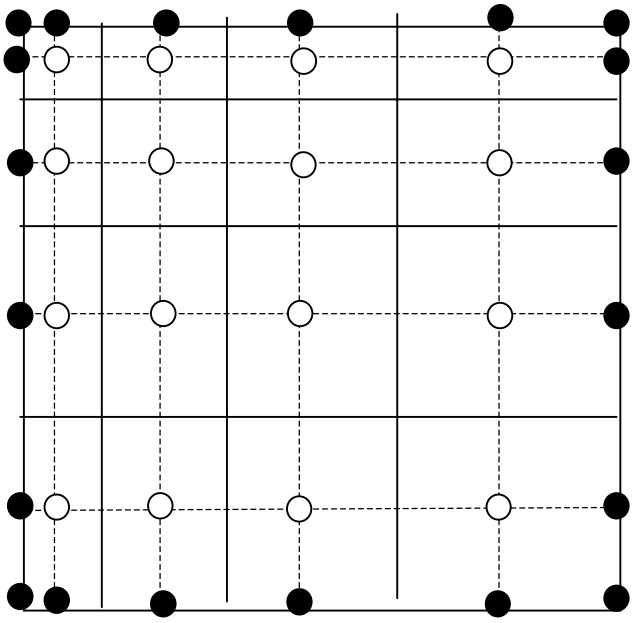

(b)

Figure 3.3.1 Types of FV grids (a) nodes centered in CVs (b) CV faces centered between nodes

The advantage of the first approach is that the nodal value represents the mean over the control volume to higher accuracy than the second approach, since the nodes are located at the center of the control volume. In the second approach,

however, central differences scheme (CDS) approximations of derivatives at control volume faces are more accurate when the face is midway between two nodes. The discretization principles are the same for the both approaches.

3.3.1 Discretization process

In this study, discretization of the flow equations within the FASTEST3D, which is introduced in Chapter 4 in detail was carried out using finite volume method.

The equations describing fluid flow are derived from the conservation of mass and momentum. General form of the conservation equations are (Versteeg, Malalasekera, 1995)

continuity: $$\frac{\partial \rho}{\partial t} + div\left(\rho \vec{v}\right) = 0 \tag{3.3.1}$$

momentum: $$\frac{\partial}{\partial t}\left(\rho \vec{v}\right) + div(\rho \vec{v}\vec{v} - \overline{\overline{T}}) = \vec{s_v} \tag{3.3.2}$$

where ρ is density, v is velocity, T is the diffusion flux vector, Equation (3.3.2) is written in terms of a velocity component U_i, obtain

$$\frac{\partial}{\partial t}\left(\rho U_i\right) + div(\rho \vec{v} U_i - \vec{t_i}) = s_{ui} \tag{3.3.3}$$

where $\vec{t_i}$ is the momentum diffusion and s_{ui} is the source term which represent the external forces;

$$\vec{t_i} = \tau_{ij}\vec{i_j} \tag{3.3.4}$$

$$s_{ui} = -\frac{\partial P}{\partial y^i}\ ,\ P = p + \rho g h \tag{3.3.5}$$

The index 'i' denotes the direction of the Cartesian coordinate. U_i are the Cartesian velocity components, p is the pressure, g is the gravity constant and h the distance from a given reference level. τ_{ij} are the anisotropic parts of the stress tensor. For a Newtonian fluid and incompressible laminar flow it can be expressed as the product of the dynamic viscosity and the rate of strain as:

$$\tau_{ij} = \mu\left(\frac{\partial U_i}{\partial y^j} + \frac{\partial U_j}{\partial y^i}\right) \tag{3.3.6}$$

Figure 3.2 shows the Cartesian coordinate system $\left(y^1, y^2\right)$ with base vector $\vec{i}_1$ and $\vec{i}_2$ and a typical control volume. Equation (3.3.1) and (3.3.2) are to be integrated over a finite number a control volumes and over the time interval $\left(t_{l-1}, t_l\right)$.

Here, Divergence theorem is used, which transforms the volume integral of a vector divergence in to a surface integral:

$$\int_v div\,\vec{f}\,dV \equiv \int_A \vec{f}\,\vec{d}A \tag{3.3.7}$$

V is the volume of the control volume and A is the area of its surface, $\vec{d}A$ being the outward directed surface vector normal to this surface. The right hand side of the equation (3.3.7) represents the net flux of the transport quantity through the control volume surface. It must be equal to the net source given by the right hand side of equations (3.3.1) and (3.3.2). In the case of the continuity equation, there is no source term, i.e. mass is conserved, so the net mass flux must be zero. For the momentum equations the right hand side $\left(s_{ui}\right)$ represents the external forces.

The surface integrals are evaluated on each control volume face and then summed up. For a two dimensional case the third dimension is unity, and the fluxes

in this direction are zero. Since the third dimension is unity the cell face areas are equal to the length of the line segments connecting the two vertices.

The fluxes are by definition equation (3.3.7) taken positive when directed outwards. Outward flux through the 'e' or east cell face (Figure 3.3.2), I_e, is the inward flux through the 'w' or west cell face of the neighbor control volume can be expressed as : $(I_e)_P = (-I_w)_E$. Therefore only two fluxes per control volume need to be calculated, namely I_e and I_n. The general form of the discretized equation then becomes:

$$I_e + I_w + I_n + I_s = S \tag{3.3.8}$$

where the I's represent the fluxes through respective cell surfaces. Similarly subscripts n and s denotes the quantities in the north and south directions as shown in the Figure 3.3.2.

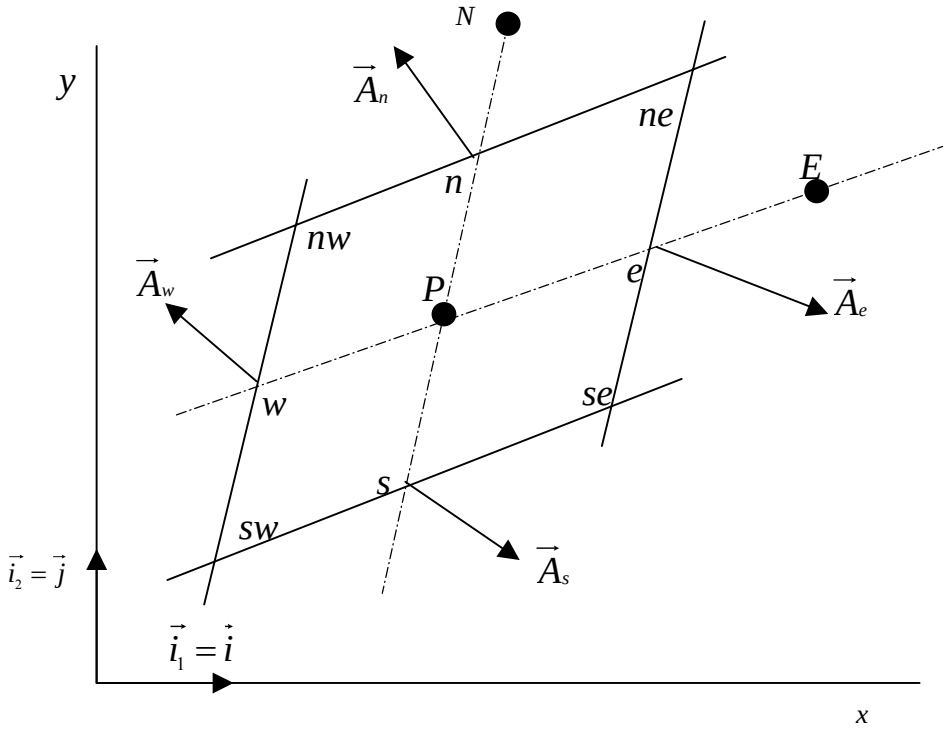

Figure 3.3.2. A typical control volume and the notation used for a Cartesian 2D grid

$$I_e = \int_{Ae} \vec{f}.\vec{d}A \approx \vec{f}_e.\vec{A}_e \tag{3.3.9}$$

The surface vectors on the cell faces are defined as:

$$\vec{A}_e = \left(y_n - y_s\right)_e \vec{i} - \left(x_n - x_s\right)_e \vec{j} \tag{3.3.10}$$

$$\vec{A}_n = \left(y_w - y_e\right)_n \vec{i} - \left(x_w - x_e\right)_n \vec{j} \tag{3.3.11}$$

where x's and y's stand for the horizontal and vertical positions of the cross-sectional points of the surfaces, respectively. In the case of the continuity equation, the vector $\vec{f}$ in equations (3.3.7) and (3.3.9) stands for $\rho\vec{v}$. The positive, outward directed fluxes through the east and north cell faces become:

$$I_e = F_{1e} = \int_{Ae} \rho\vec{V}.\vec{d}A \approx \left(\rho\vec{V}.\vec{A}\right)_e = \rho_e\left[U\left(y_n - y_s\right) - V\left(x_n - x_s\right)\right]_e \tag{3.3.12}$$

$$I_n = F_{2n} = \int_{An} \rho \vec{V}.\vec{d}A \approx \left(\rho \vec{V}.\vec{A}\right)_n = \rho_n \left[U\left(x_e - x_w\right) - V\left(y_e - y_w\right)\right]_n \qquad (3.3.13)$$

F_1 and F_2 denote the average mass fluxes in the positive direction of general coordinate x^1 and x^2 respectively. U and V are the x and y components of the velocity, respectively. The continuity equation then becomes

$$F_{1e} - F_{1w} + F_{2n} - F_{2s} = 0 \qquad (3.3.14)$$

U_e, V_e, U_n and V_n in equations (3.3.12) and (3.3.13) represent the average values of the Cartesian velocity components at the appropriate cell faces.

The left hand side of the momentum equations (3.3.3) has two parts: convection and diffusion. For the convection fluxes I^C, $\vec{f}$ in equations (3.3.7) and (3.4.9) is substituted by $\rho U \vec{v}$, yielding:

$$I_e^C \approx F_{1e} U_e \qquad (3.3.15)$$

$$I_n^C \approx F_{2n} U_n \qquad (3.3.16)$$

In case of the diffusion fluxes I^D, the vector $\vec{f}$ stands in the U equation for $-\vec{t}_1$, yielding:

$$I_e^D \approx -(\tau_{11}\vec{i} + \tau_{12}\vec{j})_e.\vec{A}_e \qquad (3.3.17)$$

$$I_n^D \approx -(\tau_{11}\vec{i} + \tau_{12}\vec{j})_n.\vec{A}_n \qquad (3.3.18)$$

The stresses τ_{11} and τ_{12} contain velocity derivatives with respect to Cartesian coordinates, these have to be expressed in term of general coordinate ξ^i, according to :

$$\frac{\partial U}{\partial x}=\frac{1}{J}\left(\frac{\partial y}{\partial \eta}\frac{\partial U}{\partial \xi}-\frac{\partial y}{\partial \xi}\frac{\partial U}{\partial \eta}\right) \tag{3.3.19}$$

$$\frac{\partial U}{\partial y}=\frac{1}{J}\left(\frac{\partial x}{\partial \xi}\frac{\partial U}{\partial \eta}-\frac{\partial x}{\partial \eta}\frac{\partial U}{\partial \xi}\right) \tag{3.3.20}$$

where J is the Jacobian of the coordinate transformation $(x,y)=f(\xi,\eta)$ defined by:

$$J=\frac{\partial x}{\partial \xi}\frac{\partial y}{\partial \eta}-\frac{\partial x}{\partial \eta}\frac{\partial y}{\partial \xi} \tag{3.3.21}$$

The Jacobian and derivatives of the equations (3.3.19) and (3.3.20) need to be evaluated at the cell face locations ‘e’ and ‘n’. For the ‘e’ face, the ξ coordinate is taken to connect the points P and E (from P to E) and η runs along the ‘e’ cell face (from the ‘se’ to ‘ne’). The derivatives $\frac{\partial x}{\partial \xi}$, $\frac{\partial x}{\partial \eta}$ can be approximated as:

$$\left(\frac{\partial x}{\partial \xi}\right)_e \approx \frac{x_E-x_P}{\xi_E-\xi_P}\ ;\ \left(\frac{\partial x}{\partial \eta}\right)_e \approx \frac{x_{ne}-x_{se}}{\eta_{ne}-\eta_{se}} \tag{3.3.22}$$

For the simplicity, $\xi_E-\xi_P$ is taken $l_{P,E}$ which is the distance between point P and E; analogously, $\eta_{ne}-\eta_{se}$ is set equal to the $l_{ne,se}$, the length of the cell face between vertices ‘ne’ and ‘se’. The Jacobian can then approximated by:

$$J_e \approx \frac{1}{l_{P,E}l_{ne,se}}\left[(x_E-x_P)(y_n-y_s)_e-(x_n-x_s)_e(y_E-y_P)\right] \tag{3.3.23}$$

The derivatives in equations (3.3.19) and (3.3.20) can be expressed via expression equations (3.3.22) and (3.3.23) to yield:

$$\left(\frac{\partial U}{\partial x}\right)_e \approx \frac{(y_n-y_s)_e(U_E-U_P)-(y_E-y_P)(U_n-U_s)_e}{(y_n-y_s)_e(x_E-x_P)-(y_E-y_P)(x_n-x_s)_e} \tag{3.3.24}$$

$$\left(\frac{\partial U}{\partial y}\right)_e \approx \frac{(U_n - U_s)_e (x_E - x_P) - (U_E - U_P)(x_n - x_s)_e}{(y_n - y_s)_e (x_E - x_P) - (y_E - y_P)(x_n - x_s)_e} \tag{3.3.25}$$

When the expression (3.3.6) for τ_{ij} are introduced in equations (3.3.17-18) and relations of the form (3.3.24-25) are used the following expression can be written as for the diffusion fluxes I_e^D and I_n^D:

$$\begin{aligned} I_e^D \approx & -\frac{\mu_e}{\delta V_e}\{(U_E - U_P)\left[2(y_n - y_s)_e^2 + (x_n - x_s)_e^2\right] - \\ & (U_n - U_s)_e\left[2(y_E - y_P)(y_n - y_s)_e + (x_E - x_P)(x_n - x_s)_e\right] - \\ & \left[(V_E - V_P)(y_n - y_s)_e - (V_n - V_s)_e (y_E - y_P)\right](x_n - x_s)_e\} \end{aligned} \tag{3.3.26}$$

$$\begin{aligned} I_n^D \approx & -\frac{\mu_n}{\delta V_n}\{(U_N - U_P)\left[2(y_e - y_w)_n^2 + (x_e - x_w)_n^2\right] - \\ & (U_e - U_w)_n\left[2(y_N - y_P)(y_e - y_w)_n + (x_N - x_P)(x_e - x_w)_n\right] - \\ & \left[(V_N - V_P)(y_e - y_w)_n - (V_e - V_w)_n (y_N - y_P)\right](x_e - x_w)_n\} \end{aligned} \tag{3.3.27}$$

It should be noted that the outward diffusion flux thorough the 'e' cell face is the inward flux through the 'w' cell face of the neighbor control volume that is $(I_w^D)_P = (-I_e^D)_w$ and $(I_s^D)_P = (-I_n^D)_S$; also δV_n and δV_e are defined as the scalar product of the surface vector $\vec{A}_n$ and $\vec{A}_e$ respectively.

$$\delta V_n = \vec{A}_n . \overline{PN} = -(y_e - y_w)_n (x_N - x_P) + (x_e - x_w)_n (y_N - y_P) \tag{3.3.28}$$

$$\delta V_e = \vec{A}_e . \overline{PE} = -(y_n - y_s)_e (x_E - x_P) + (x_n - x_s)_n (y_E - y_P) \tag{3.3.29}$$

For the V -momentum equation, the convection and diffusion fluxes are obtained as:

$$I_e^C \approx F_{1e} V_e \tag{3.3.30}$$

$$I_e^C \approx F_{2n} V_n \tag{3.3.31}$$

and

$$\begin{aligned} I_e^D \approx & -\frac{\mu_e}{\delta V_e}\{(V_E - V_P)\left[2(y_n - y_s)_e^2 + (x_n - x_s)_e^2\right] - \\ & (V_n - V_s)_e\left[2(x_E - x_P)(x_n - x_s)_e + (y_E - y_P)(y_n - y_s)_e\right] - \\ & \left[(U_n - U_s)_e(x_E - x_P) - (U_E - U_P)(x_n - x_s)_e\right](y_n - y_s)_e\} \end{aligned} \tag{3.3.32}$$

$$\begin{aligned} I_n^D \approx & -\frac{\mu_n}{\delta V_n}\{(V_N - V_P)\left[2(x_e - x_w)_n^2 + (y_e - y_w)_n^2\right] - \\ & (V_e - V_w)_n\left[2(x_N - x_P)(x_e - x_w)_n + (y_N - y_P)(y_e - y_w)_n\right] - \\ & \left[(U_e - U_w)_n(x_N - x_P) - (U_N - U_P)(x_e - x_w)\right](y_e - y_w)_n\} \end{aligned} \tag{3.3.33}$$

The source term in the momentum equations are integrated over the control volume;

$$S = \int_V s_u dV \approx (s_u)_P \delta V \tag{3.3.34}$$

Thus, the gradients $\frac{\partial P}{\partial x}$ and $\frac{\partial P}{\partial y}$ need to be evaluated at point P by analogy

to equations (3.4.19-20-21) and (3.4.23), these gradients are calculated as:

$$\left(\frac{\partial P}{\partial x}\right)_P \approx \frac{(P_e - P_w)(y_n - y_s) - (P_n - P_s)(y_e - y_w)}{(x_e - x_w)(y_n - y_s) - (x_n - x_s)(y_e - y_w)} \tag{3.3.35}$$

$$\left(\frac{\partial P}{\partial y}\right)_P \approx \frac{(P_n - P_s)(x_e - x_w) - (P_e - P_w)(x_n - x_s)}{(x_e - x_w)(y_n - y_s) - (x_n - x_s)(y_e - y_w)} \tag{3.3.36}$$

Source terms for the momentum equations can be approximated as:

$$S_u^p \approx -(P_e - P_w)(y_n - y_s) + (P_n - P_s)(y_e - y_w) \tag{3.3.37}$$

$$S_v^p \approx -(P_n - P_s)(x_e - x_w) + (P_e - P_w)(x_n - x_s) \tag{3.3.38}$$

When all the flux components and the discretized sources are introduced in equation (3.4.8), an algebraic counterpart of the differential equation is obtained.

$$[A]\{\phi\} = \{S\} \tag{3.3.39}$$

where $[A]$ is the $M \times M$ matrix, M is the total number of the control volumes, $\{\phi\}$ is the dependent variable vector of M nodal values and $\{S\}$ is similar vector containing source terms.

3.4 Solution Methods

The previous discussion showed the partial differential equations may be discretized using FV method. The result of the discretization process is a system of algebraic equations, which are linear or nonlinear according to the nature of partial differential equations from which they are derived.

Two methods are available for the solution of linear algebraic equations: the direct and iterative methods. In non-linear case, the discretized equations must be solved by using iterative technique.

3.4.1 Direct methods

Direct methods are based on a finite number of arithmetic operations leading to the exact solution of a linear algebraic system in one step.

3.4.1.1 Gauss elimination

The basic method for solving linear systems of algebraic equations is Gauss elimination. Its basis is the systematic reduction of large systems of equations to smaller ones (Heath, 1997).

$$A=\begin{pmatrix} a_{11} & a_{12} & a_{13} & \dots & a_{1n} \\ a_{22} & a_{22} & a_{23} & \dots & a_{2n} \\ \vdots & \vdots & \vdots & \ddots & \vdots \\ a_{n1} & a_{n2} & a_{n3} & \cdots & a_{nn} \end{pmatrix} \tag{3.4.1}$$

The base of the algorithm is the technique for eliminating below the diagonal matrix element that is replacing it with zero. After this operation, the original matrix is replaced by the upper triangular matrix:

$$U=\begin{pmatrix} a_{11} & a_{12} & a_{13} & \dots & a_{1n} \\ 0 & a_{22} & a_{23} & \dots & a_{2n} \\ \vdots & \vdots & \vdots & \ddots & \vdots \\ 0 & 0 & 0 & \cdots & a_{nn} \end{pmatrix} \tag{3.4.2}$$

After this step all of the elements except in the first row differ from in the original matrix A. Triangular linear systems are solved by successive substitution process, which is called back-substitution.

3.4.1.2 Tridiagonal systems

A finite difference approximation provides an algebraic equation at each grid node. Each equations contains only the variable at its own node and its left and right neighbors as shown in Figure 3.4.1.2.1.

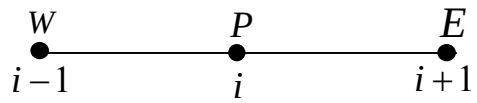

Figure 3.4.1.2.1. 1 D Cartesian grid for FD methods

$$A_W^i\phi_{i-1}+A_P^i\phi_i+A_E^i\phi_{i+1}=Q_i \tag{3.4.3}$$

The corresponding matrix A has non zero terms only on its main diagonal and the diagonal above and below it. Such matrix is called tridioganal shown Figure 3.4.1.2.2.

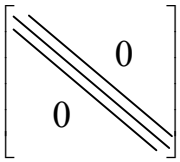

Figure 3.4.1.2.2. Schematic representation of the tridioganal matrix

Gauss elimination is preferred for solving tridioganal systems since only one element needs to be eliminated from each row during the forward elimination process.

3.4.2 Iterative methods

The basis of iterative methods is to perform a small number of operations on the matrix element of the algebraic system, the aim of approach in the exact solution within a preset level of accuracy and small number of iteration. A large number of iterative methods are available some of these are:

1) Jacobi method
2) Gauss-Seidel method
3) Successive over relaxation (SOR) method
4) Alternating direction implicit (ADI) method
5) Strongly implicit procedure (SIP)
6) Conjugate gradient method
7) Multi grid method

3.4.3 Solution of the non-linear equations

There are two types techniques for solving non linear equations: Newton-like and global. Newton-like techniques are much faster when a good estimate of solution is available but global techniques ensure the solution to converge.

3.5 Convergence Criteria

When using iterative solvers, it is important to know when to stop. The most common procedure is based on the difference between two successive iterates; the procedure is stopped when this differences, measured by some norm, is less that pre selected value.

The numerical solution u_i^n should approach the exact solution $\bar{u}(x,t)$ of the differential equations at any points $x_i = i\Delta x$ and time $t_n = n\Delta t$ when Δx and Δt tend to zero, that is, when the mesh is refined x_i and t_n being fixed. This condition implies that i and n goes to infinity while Δx and Δt goes to zero (C. Hirssch, 1997). This condition for convergence of the numerical solution to the exact solution of the differential equation express that the error,

$$\bar{\varepsilon}_i^n = u_i^n - \bar{u}(i\Delta x, n\Delta n)$$

satisfies the following convergence condition;

$$\lim_{\substack{\Delta t\to 0 \\ \Delta x\to 0}} \left|\varepsilon_i^n\right| = 0 \text{ at fixed values of } x_i = i\Delta x \text{ and } t_n = n\Delta t .$$

3.6 Numerical Methods in Our Study

Numerical techniques described above are all of the methods which can be used for solution of any mathematical model based on computational fluid dynamics. In our study for the discretization of the incompressible Navier-Stokes equations in

time and space, finite volume method was used and block structured grid was selected because of the easy treatment of the complex geometry. At the end of the discretization process, linear algebraic equation was obtained and this matrix equation solved by using strongly implicit SIP method of Stone time integration by second order Crank-Nicolson scheme. The inherently time-dependent geometry of stirred vessel is simulated by a multiple frame of reference approach which is mentioned in Chapter 4.

Besides of these numerical techniques, for the treatment of the rotating impeller in mixing tank some new methods have been introduced. Detailed information is given in the following parts.

3.7 Numerical Methods Used In Mixing Applications

Improvements in computer hardware and capacity of the memory resulting in developed of predictive methods based on computational fluid dynamics (CFD) and capable of providing detailed information not only flow and turbulence field but also impeller performance characteristics like impeller power number and pumping number in the stirred tank.

In the past most of the studies for the flow simulations in the stirred tanks are based on steady-state analyses (Harvey and Greaves, 1982), (Ranade and Joshi, 1989), (Bakker, 1992). Most of these investigators have treated the rotating impeller as a black box, since this approach requires boundary condition in the immediate vicinity of the impeller, which must be determined experimentally. Though this approach was successful in the prediction of the flow characteristics in the bulk of the tank, but it was restricted to the conditions for which input data are available are

not for true predictions. Since a single set of impeller boundary conditions must be used for geometrically similar systems, it cannot be used large number alternative mixer configurations

To overcome limitations associated with the requirement of the experimental impeller boundary conditions, recently some methods have been developed. These methods are namely momentum source, snapshot, sliding mesh and multiple frame of reference method which was used in this study.

3.7.1 Impeller models

As mentioned above, there are four different approaches for the modeling of the impeller. They are analyzed in further detailed below especially focus on clicking method.

3.7.1.1 Momentum source method

Momentum source model is based on aerofoil aerodynamics. In this model, the impeller blades are replaced with finite blade section by dividing the blade into a number of vertical strips from the hub to tip (Xu and McGrath, 1996), (Pericleous and Patel, 1987). The blade sections inside each strip are approximated to an aerofoil and aerofoil aerodynamics is applied. No experimental data are required in this model but it is restrictive since the flow inside the impeller is assumed to have no azimuthal direction of the flow between the blades.

3.7.1.2 Snapshot method

In the snapshot method, impeller blades are fixed at one particular position with respect to the baffles. This method can be explained as follows: in a real case rotation of the blade causes suction of fluid at the back side of the impeller blades and equivalent ejection of fluid from the front side of the blades. These phenomena

of ejection and suction have been modeled by snapshot formulation (Ranade and Dommeti, 1996). That is, computational cells adjacent to the back side of the blades are modeled by specifying the mass sources, it can be defined as:

$$S_m = -\rho A_{bc} W_{bc} \qquad (3.7.1.2.1)$$

where A_{bc} and W_{bc} are the area of the surface of the computational cell which is the adjacent to the impeller blade. For the computational cell on the back side of the blades are modeled by specifying the mass sinks and it is defined by expression (3.7.1.2.1) with the positive sign

$$S_m = \rho A_{bc} W_{bc} \qquad (3.7.1.2.2)$$

3.7.1.3 Sliding mesh method

In the sliding mesh method, the tank is dividing in to two regions that are impeller region and the tank region. The tank region includes the bulk of the liquid, the tank wall, the tank bottom and the baffles. The grid in the impeller region rotates with the impeller while the grid in the tank remains stationary (Bakker et al., 1996), (Lane and Koh, 1997), (Jaworski et al., 1997), (Lee and Yanneskis, 1996). The two grids slide past each other at a cylindrical interface. Two regions are implicitly coupled at the interface via a sliding mesh algorithm which takes in to account the relative motion between the two sub-domains and performs the conservative interpolation.

CHAPTER 4

NUMERICAL METHOD FOR SOLVING TIME DEPENDENT FLUID DYNAMICS

4.1 Numerical Methods

In this section numerical method and tools used in the flow simulations are explained. In the past most of the studies for the flow simulations in the stirred tanks are based on steady-state analyses as outlined in chapter 3. This technique, however, needs some experimentally obtained boundary conditions in the vicinity of the impeller. Therefore this method is not practical to study large number of impeller configuration.

To overcome limitations associated with the requirement of the experimental impeller boundary conditions, recently some methods have been developed. These methods are as previously described as momentum source method, snapshot method and sliding mesh method. Another method being used in the mixing simulations is multiple frame of reference method, which is the technique employed in this study due to some shortcomings of the mentioned alternative methods. For example in the momentum source method the impeller modeling is rather restrictive because the flow inside the impeller is assumed to have no azimuthal direction variations, so there is no straight forward simulation of the flow between the blades. The snapshot technique provides a relatively less computational intensive for the simulation of flow between impeller blades. Finally, the sliding mesh method is based on the time dependent laminar flow simulation only. It is also highly CPU time demanding.

4.1.1 Multiple frame of reference method

In this study all of the numerical simulations are carried out by using multiple frame of reference with clicking method within the FASTEST3D code. In this method tank is divided into two frames. These are rotating frame and stationary frame. Rotating reference frame encompasses the impeller and the flow surrounding it and stationary frame includes the tank, the baffles and the flow outside the impeller frame. Figure 4.1.1.1 depicts the configuration used. This figure shows that the tank is formed by twenty three blocks, seventeen blocks of them are defined as rotating which are represented by the red color blocks and remaining are six stationary blocks, which are indicated by yellow color. Interface blocks are not physically defined by the user when the grid generation is being constructed. These blocks are defined by the program as an imaginary section to provide the interaction between the rotating and stationary blocks. The interface blocks are represented by dark blue and light blue as shown in Figure 4.1.1.2. Numbers of the control volumes which are forming the interface blocks belonging to stationary and rotating parts are equal at θ direction. In the stationary blocks, governing equations are the common equation of continuity and Navier Stokes equations. In the flow region surrounding the impeller those governing equations are modified for the rotating frame.

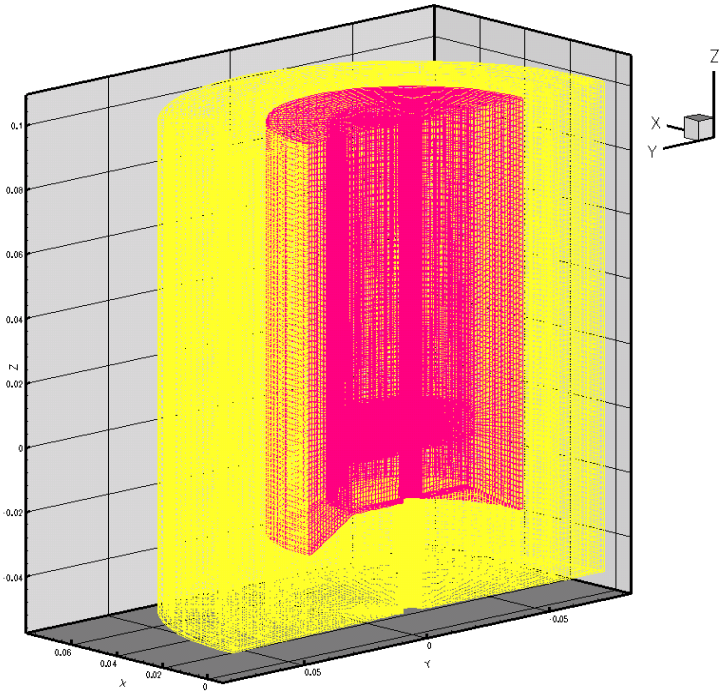

Figure 4.1.1.1 Rotating and stationary blocks in the solution domain

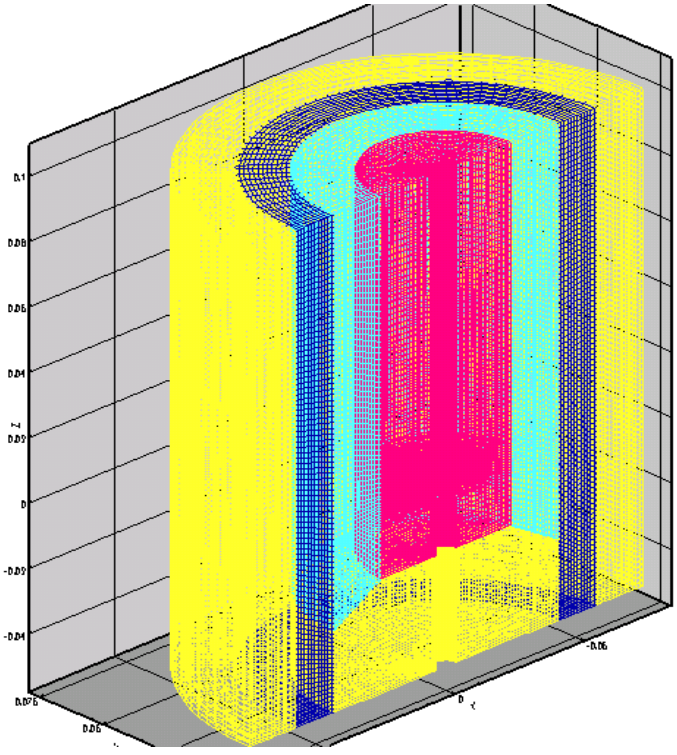

Figure 4.1.1.2 Interface sections of the stationary and rotating blocks

In this method clicking step size and number of the time step have to be defined by user before executing the program. Once the flow quantities such as velocities and pressures are determined for a certain control volume near the impeller, for the next time step those quantities are transferred as initial condition to the other control volume which is in front of the original control volume by the clicking step size in the rotation direction. Therefore, by this procedure rotation around the impeller is mimicked. Once the clicking step size and angular velocity are set by the user, time step is calculated according to those values by the code.

In this study the investigated tank is divided into two symmetric parts as shown in Figure 4.1.1.3 to reduce the computational requirements. Each part consists of two baffles and three impeller blades. The clicking step size is set as two and times step number depending on the Reynolds number varies between 3000 and 6000. Rotating blocks are jumped by two control volumes in the r-θ plane. Since there are 48 control volumes at the defined interface of the rotating block in θ direction, it takes 24 time steps to complete 180 degree (two clicking step size is corresponding to 7.5 degree) revolution of the impeller blade. Eventually solutions of the two frames at the interface are performed via velocity transformation from one frame to other. Investigation of the 180 degree of the tank in θ direction is assumed to be sufficient to study whole tank due to the symmetry. Figure 4.1.1.4 shows the impeller location after the different time steps

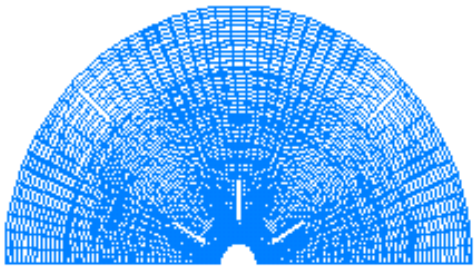

Figure 4.1.1.3 Grid distribution in r-θ plane

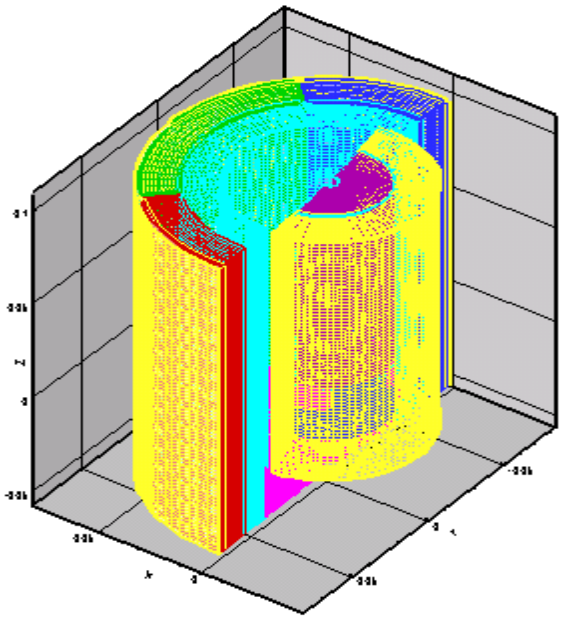

(a) After first time step

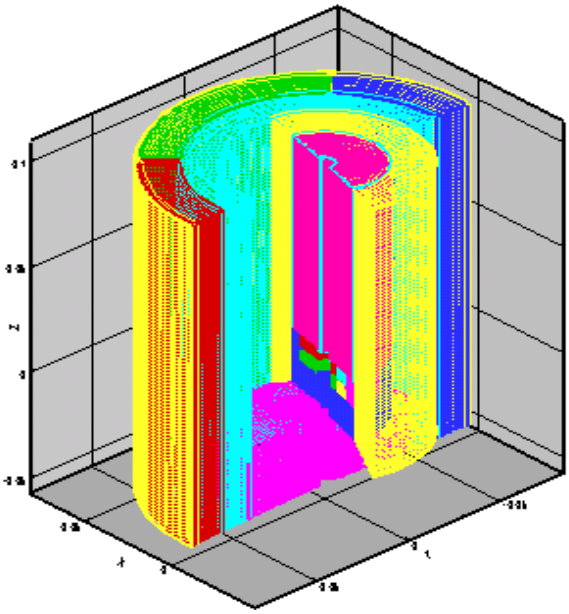

(b) After 10. time step

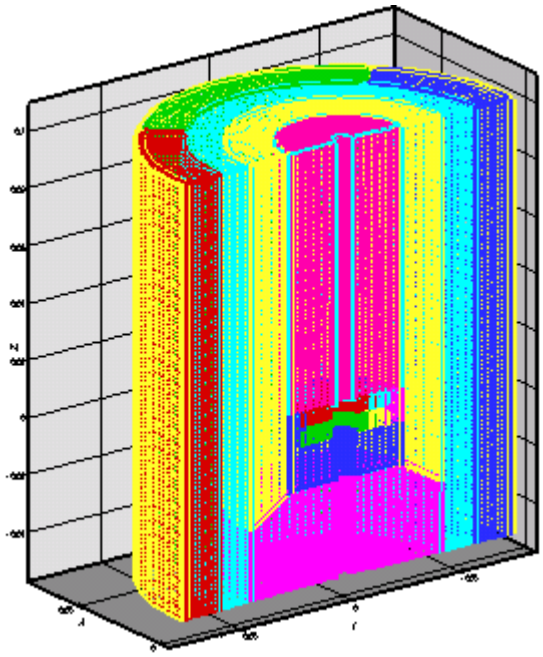

(c) After 24. time step

Figure 4.1.1.4 Impeller locations after different time steps

4.2 FASTEST3D

In this study all numerical simulations are carried out by using FASTEST3D code. FASTEST is an abbreviation for 'Flow Analysis by Solving Transport equations Simulating Turbulence.' It has been developed at the university of Erlangen-Nuremberg. FASTEST3D was written by using Fortran language and it works under the Linux operating system.

The complete FASTEST3D program consists of there computer sub programs:

1) A pre-processor for generating the numerical grid,
2) A flow predictor,
3) A post-processor for the graphical visualization of the result.

A typical FASTEST3D operation can be summarized as follows: Firstly a grid is generated by taking into account the shape and size of the tank and impeller. Details of this process are being explained under the topic of the grid generation and parameters. Other parameters such as angular velocity, fluid properties, clicking step size and time step number are also supplied to the code. The code then solves the mixing problem and produces quantities characterizing the flow field in the tank such as velocity components, turbulence and pressure quantities and power consumption as shown in Figure 4.2.1.

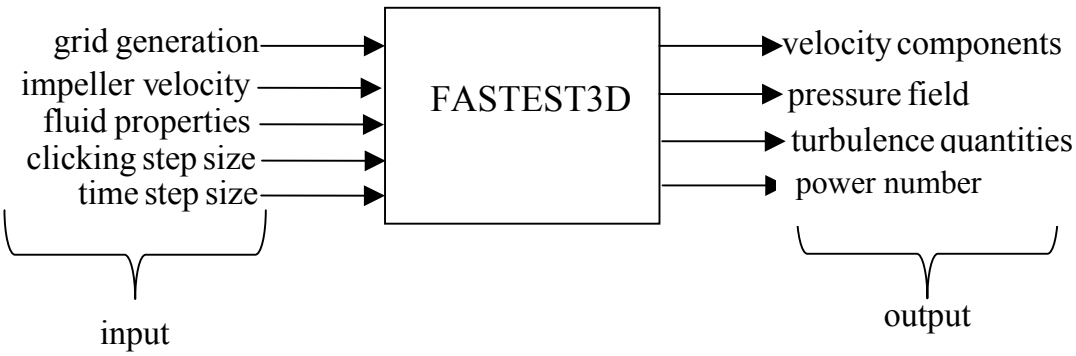

Figure 4.2.1 Flow chart of the running FASTEST

FASTEST3D is a flexible code that can be modified according to the specific fluid flow problems. Its major drawback is that it is not user friendly and to master the code one needs a lot of practice and trial-error

4.3 Grid generation

For the treatment of complex geometries like mixing tank, block structured irregular grid is used in FASTEST3D. These globally unstructured, but locally structured grids can be viewed as a compromise between the flexibility of fully unstructured grids and numerical efficiency of globally structured grids. Figure 4.3.1 shows a block structured grid which is used in this study. Solution domain is divided

into symmetric parts. Each one encompassing two baffles and three impeller blades (Figure 4.3.2). Our solution domain consists of 23 blocks and total number of computational cells used is 248020. Table 4.3.1 shows number of control volume in the blocks-.

Table 4.3.1 Number of the control volumes in the blocks

Block number	θ	r	z	Number of control volumes
Block 1:	7×	5×	5=	175 CVs
Block 2:	7×	5×	5=	175 CVs
Block 3:	7×	5×	12=	420 CVs
Block 4:	14×	5×	5=	350 CVs
Block 5:	14×	5×	5=	350 CVs
Block 6:	14×	5×	12=	840 CVs
Block 7:	14×	5×	5=	350 CVs
Block 8:	14×	5×	5=	350 CVs
Block 9:	14×	5×	12=	840 CVs
Block 10:	7×	5×	5=	175 CVs
Block 11:	7×	5×	5=	175 CVs
Block 12:	7×	5×	12=	420 CVs
Block 13:	48×	5×	5=	1200 CVs
Block 14:	48×	5×	5=	1200 CVs
Block 15:	48×	17×	10=	8160 CVs
Block 16:	48×	17×	52=	42432 CVs
Block 17:	48×	15×	74=	52380 CVs
Block 18:	48×	32×	20=	30720 CVs

Table 4.3.1 Number of the control volumes in the blocks continued.

Block number	θ	r	z	Number of control volumes
Block 19:	12×	10×	94=	11280 CVs
Block 20:	23×	10×	94=	21620 CVs
Block 21:	11×	10×	94=	10340 CVs
Block 22:	48×	12×	94=	54144 CVs
Block 23:	48×	2×	94=	+ 9024 CVs
Total				248020 CVs

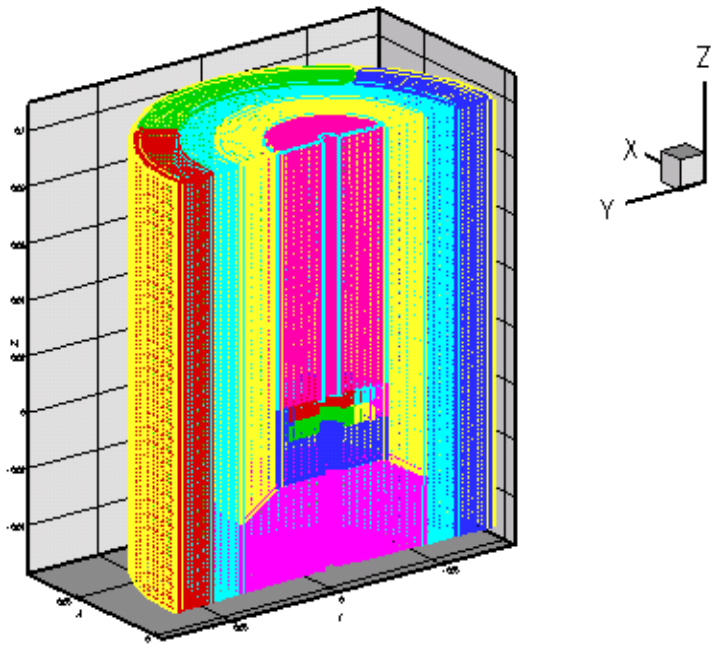

Figure 4.3.1 Block structured irregular grid.

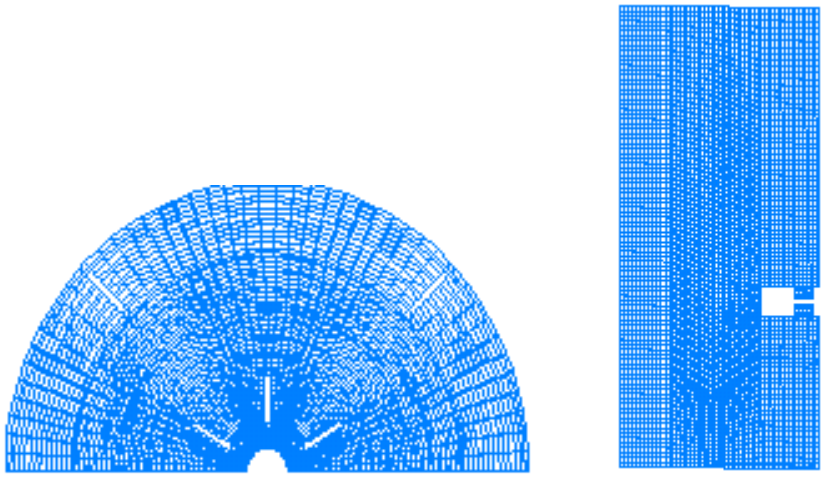

(a) (b)

Figure 4.3.2 Grid distribution (a) typical r- θ plane (b) typical r-z plane

One of the advantages of the using block structured grid is generating needed number of the solution domain. The important point in the treatment of the complex geometries like stirred tank with baffles is taking large numbers and small size of control volumes in the vicinity of the impeller where changes in the flow quantities occur rather in a smaller length scales compared to the other regions in the tank. Up to now most of the studies have been based on structured grid and block structured grid has not been used in the field of mixing. The other advantage of the block structured grid is that it is well suited as a base for the parallelization of the computational by means of grid partitioning techniques.

4.3.1 Geometry parameters

The selected standard tank configuration with Rushton turbine is shown in Figure 4.3.1.1. All of the geometrical quantities are expressed in terms of tank diameter. In the case of changing any of the geometrical parameters, spatial

discretization of the new configuration is updated through the grid generation procedure.

The system investigated consists of a standard stirred cylindrical vessel (diameter=height=0.15 m) with four baffles (length=0.015 m) equally spaced around the periphery. The shaft of the impeller is concentric with the axis of the vessel. The standard six-bladed flat bladed (diameter=0.05 m) Rushton turbine impeller is located 0.05 m from bottom of the tank. Diameter and height of the hub are 0.0125 m. The diameter of the shaft is 0.008 m.

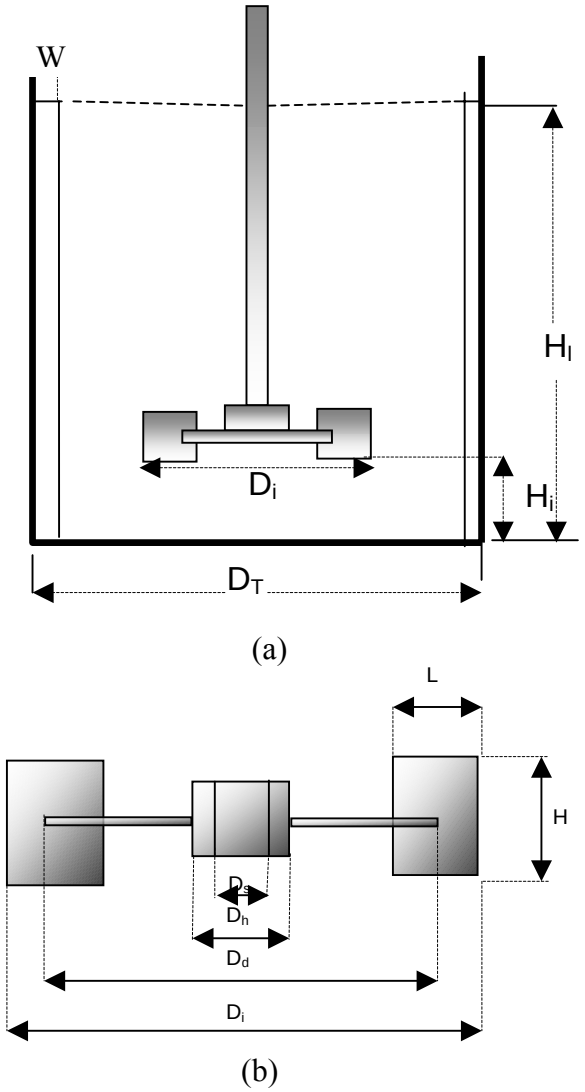

Figure 4.3.1.1 (a) A standard baffled mixing tank (b) Geometrical details of the ine impeller.

In this study, the geometrical parameters shown in Figure 4.3.1.1 are set as follows:

D_T= Tank diameter 0.15 m

D_i= Impeller diameter; $D_i = D_T/3$=0.05 m

H_l= Height of the liquid; $H_l = D_T$=0.15 m

H_i= Impeller height from bottom of the tank; $H_i = D_T/3$=0.05 m

W= Length of the baffles; $W=3D_i/10$=0.015 m

L= Length of the blade; $L= D_i/4$=0.0125 m

H=Height of the blade; $H= D_i/5$=0.01m

D_d= Diameter of the disc; $D_d=3D_i/4$=0.0375 m

D_h= Diameter of the hub; $D_h= D_i/4$=0.0125 m

D_s= Diameter of the shaft; $D_s=4D_i/25$=0.008 m

4.4 Computational requirements

Prior to the simulation, the selected numerical tools that suit best for the numerical simulation of the stirred tank have to be specified. Details of these tools and general guidelines to make a suitable selection are covered in chapter 3. Regarding this process the following steps are taken in process of setting up numerical scheme:

1) Selection of a discretization method of the equations. This implies selection between finite difference, finite element or finite volume methods as well as selection of accuracy of the spatial and, eventually time discretization.
2) Selection of a solution method for the algebraic system of equations which is obtained from discretization

3) Analysis of the selected numerical algorithm. This step concerns the analysis of the ‘qualities’ of the scheme in terms of stability and convergence properties.

Concerning the numerical method FASTEST3D to solve the incompressible Navier-Stokes equations composed of the following components: second order finite volume discretization in time and space, strongly implicit SIP method of Stone for solving a large system of linear equations and time integration by second order Crank-Nicolson scheme. The inherently time-dependent geometry of stirred vessel is simulated by a multiple frame of reference approach, which is mentioned above. Space discretization is introduced in Chapter 3 therefore here other features of the implemented numerical methods are explained.

4.4.1 Time discretization

In addition to the spatial discretization a discretization in time is required to obtain solution of the unsteady problem. Time may be regarded as an additional coordinate, therefore a special problem can be considered as sequence of levels at several times, so-called time levels as shown Figure 4.4.1.1. In contrast to spatial discretization the variable values have to be determined before moving to the next time level. New time levels are always extrapolated from the older one.

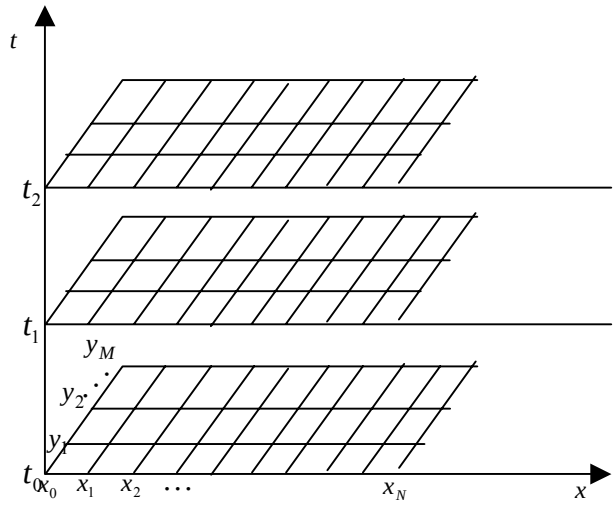

Figure 4.4.1.1 Time discretization

4.4.2 Solution method

In this study, strongly implicit (SIP) method (Stone, 1968) is used for solving linear algebraic equation systems, which are obtained from the spatial discretization process. The main reason of using SIP method is that, it provides better convergence than the other methods such as Gauss-Seidel method, conjugate gradient method and Tri-Diagonal-Matrix algorithm.

The system of discretized equations for all control volumes can be described in matrix form as

$$[A]\{\phi\} = \{S\} \tag{4.4.2.1}$$

where $[A]$ is the $M \times M$ diagonal matrix shown in Figure 4.4.2.1, M is the total number of the control volumes, $\{\phi\}$ is the dependent variable vector of M nodal values and $\{S\}$ similarly is composed of the source terms. Direct solution of such matrix equation is too costly. Using SIP method, the solution becomes less CPU

time demanding. In this method the specified matrices are by separated into upper and lowers triangular matrices (Figure 4.4.2.2).

The matrix equation then becomes

$$[C]\{\phi\} = [L][U]\{\phi\} = \{S\} \tag{4.4.2.2}$$

Therefore the solution becomes easier, since the triangular matrices can be inverted by simple forward and backward substitution. The triangular matrices $[L]$ and $[U]$ have non-zero coefficients only on diagonals which correspond to the non non-zero diagonals in the matrix $[A]$ The product matrix $[C]$ has two more diagonals than the matrix $[A]$ as shown in Figure (4.4.2.2). The coefficients of the matrix $[C]$ can be expressed through the coefficients of the $[L]$ and $[U]$ matrices, denoted by b and analogously to the coefficients a of the matrix $[A]$.

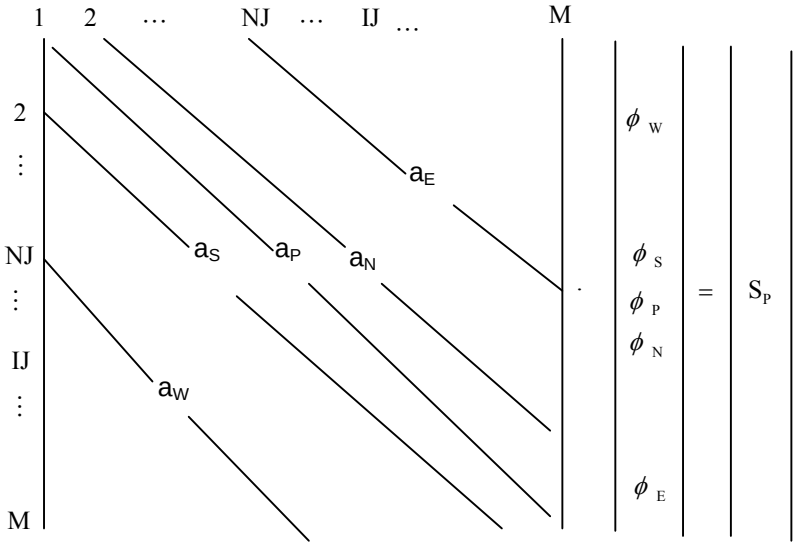

Figure 4.4.2.1 Schematic presentation of matrix equations (4.4.2.1)

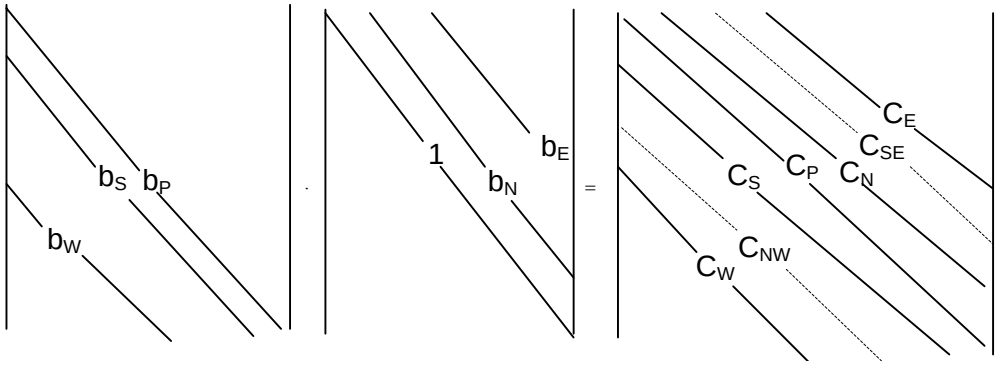

Figure 4.4.2.2 Schematic presentation of the product of triangular matrices

4.4.3 Convergence

The convergence criterion used in all simulations can be defined as follows. After the set of equations are solved and the field values are updated, new coefficients of the discretized equations are calculated. Using these new coefficients and the existing variable values, the residuals are calculated. The absolute values of the residuals for all control volumes are summed up, and this sum is normalized with an appropriate reference quantity:

- inlet mass flux for the continuity equations,
- inlet momentum flux for the momentum equations,
- mean kinetic energy for turbulent kinetic energy equation,
- mean dissipation rate for the turbulent kinetic energy dissipation rate equation.

It is then required that this normalized sum of residuals fall below a certain limit, which is defined 10^{-4} for all simulations. To examine convergence and stability, power number is calculated both on the impeller surface and in the overall tank volume. When the change in the power numbers between two successive steps is les than 1%, the solution is assumed to be converged and the program is stopped.

In the simulation at Re=10000, a time step size of 0.00521 s is used and up to 3000 time steps were performed, resulting in 62.37 revolutions to achieve the steady state flow in terms of the turbulent quantities and power number. Calculation time is approximately 5 hours per impeller revolution on a P III 1Ghz computer.

CHAPTER 5

RESULTS AND DISCUSSIONS

As mentioned before agitated vessels are used extensively in industry for conducting a variety of the processes. One of the most fundamental needs for the analysis of these processes is the knowledge of flow structure in such vessels. The flow structures are dependent on the type of agitator and other parameters like impeller clearance from the bottom of the tank and baffle length. As a result of these dependencies our investigation has focused on the effects of impeller rotational speed, N, and baffle length on the flow field and power consumption.

In this study our results consist of two parts: In the first part, we investigate the flow field generated by Rushton turbine in both laminar and turbulent regimes using Newtonian silicone oil and water as working fluids in the baffled tank, respectively. Table 5.1 shows the impeller speed, N (rpm), and corresponding impeller Reynolds numbers.

Table 5.1. Impeller speed and corresponding Reynolds number

	Water		Silicone oil		
	ρ= 1000 kg/m^3; μ=0.001 Pas		ρ=1309 kg/m^3; μ=0.0159 Pas		
Reynolds number	10000	2069	760	100	20
Impeller speed (rpm)	240	49.6	279	36,76	7,3

In the second part the effects of the baffle length on the power consumption or power number at various Reynolds numbers were considered.

5.1. Effect of the Reynolds Numbers on the Velocity Field

The flow fields obtained within the Reynolds number range from 10 to 10000 are presented in Figure 5.1.1 in the form of velocity vectors. The figure depicts the velocities in the half of the vertical cross section cut at the center of the tank. Lengths of the vectors are proportional to the magnitude of the liquid velocity. At laminar region which corresponds to Re=10, 20, 100, liquid around the impeller moves with the impeller rotation smoothly and liquid distant from the impeller is stagnant. In addition to these, two small vortex rings exist in the flow one below the impeller plane and the other above the impeller plane. In this region, the resistance to impeller rotation is mainly due to viscous effects.

Re=760, 2069 correspond to the transition region. In this region the flow around the impeller becomes unstable and turbulence sets in. Discharge flow notably increases and reaches a maximum. Now the stagnant zones which are observed in the laminar region disappear. In this region, the liquid away from the impeller is still laminar eddies start to form as a result of velocity gradients within the liquid. Also two vortex centers are observed and they get closer to the impeller plane as impeller speed is increased. No experimental results have been found in the literature for the flows in transition region so as to compare the results that were obtained in this study. Moreover, working numerically in this region is very difficult, since there is not any applicable turbulent model to the flow field at the corresponding Reynolds numbers. However, we carried out the simulations using DNS (Direct Solution of Navier Stokes Equations) method. The results obtained in this region such as velocity and power number values fit well with those results obtained in laminar and turbulent regions. Therefore the methods used in this study for the transition region may be

considered as satisfactory. Briefly the overall flow pattern in this region is irregular and flow characteristics are similar to turbulent regime.

At turbulent regime where Reynolds number is larger than 10^4 the flow pattern is highly unsteady and the large eddies form at the vicinity of the impeller plane and secondary small vortices appear in the regions away from the impeller because of the tank lid. Now stagnant zones and laminar zones, which are observed in the laminar and transition regions disappear. Discharge flow from the impeller notably increases and reaches a maximum and generates vertical circulation. As a result of this phenomena at this region mixing operation becomes highly efficient as shown in Figure 5.1.1(a). The flow field is not symmetric since the impeller is not symmetrically located with respect to vertical position. Its location is one third of the tank diameter from the tank bottom.

Through the simulations the flow field is determined for the entire tank. The details of the flow characteristics for any given location in the tank are readily available. In the forthcoming sections, on the other hand, flow field in various vertical and horizontal cross-sections of the tank is considered only for the sake of simplicity. Those locations are mainly regions around the impeller, which have the most important impact on the overall flow field.

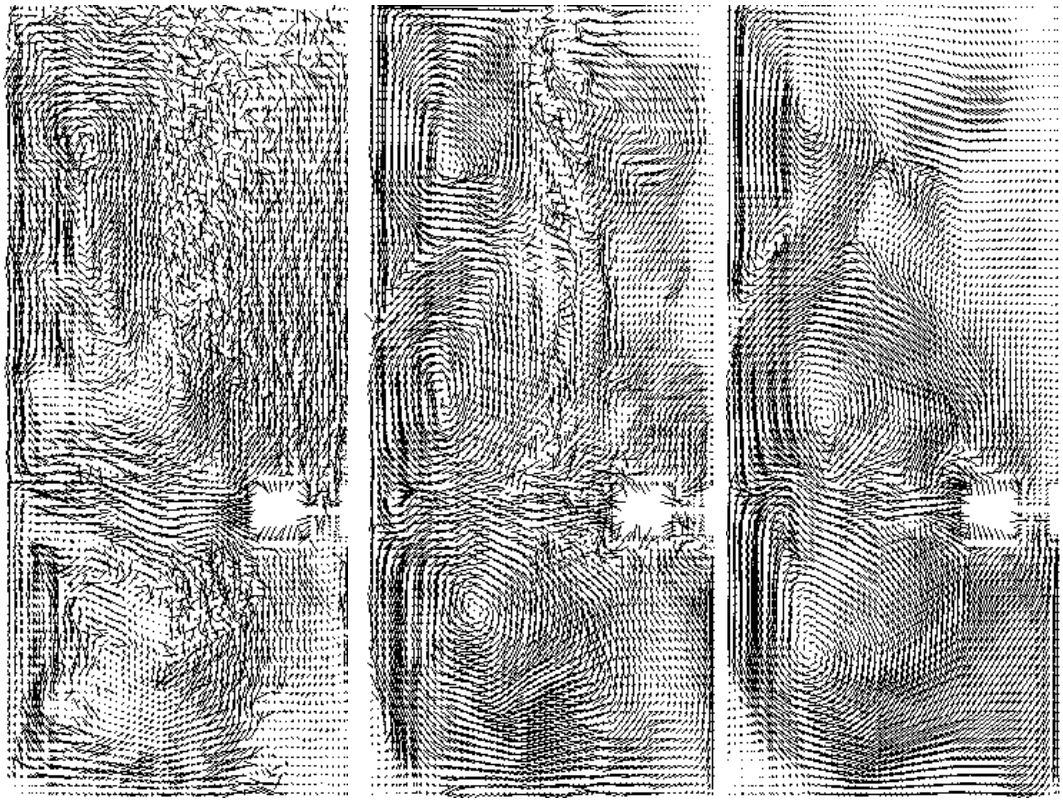

(a) (b) (c)

Figure 5.1.1. Predicted flow field on r-z plane for the standart tankconfigurations(a)Re=10000; (b) Re=2069; (c) Re=760; (d)Re=100; (e) Re=20; (f) Re=10

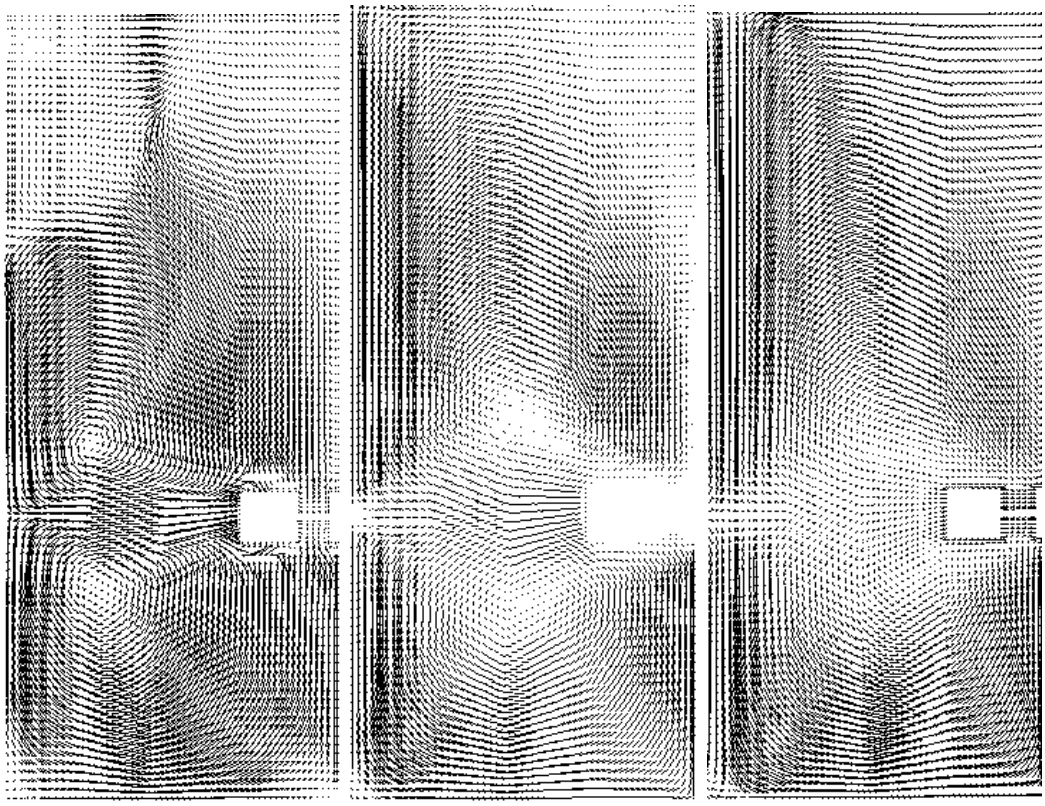

(d) (e) (f)

Figure 5.1.1. (continued)

5.1.1 Flow pattern in the radial direction

Radial, axial and tangential velocities are also investigated quantitatively at Reynolds numbers. In addition, values of effective turbulent intensity like turbulent kinetic energy and turbulent dissipation rate are calculated at Reynold number 10000 and plotted with respect to the radial and axial positions.

The radial velocities are calculated along the impeller blade height in axial direction at different radial positions, which are normalized by the impeller radius (R) as shown in Figure 5.1.1.1. Figure 5.1.1.2 depicts the radial velocities at different Reynolds numbers. In this figure horizontal axis denotes radial velocity component which is normalized by the impeller tip speed (πND_i), vertical axis, on the other hand, represents axial position, which is normalized with the impeller blade height (b) (see Figure 5.1.1.2).

Generally, the center-line radial velocity decreases with increasing radial distance from impeller which is in agreement with the experimental results from literature (Wu and Patterson, 1988; Dyster et al., 1993). At high Reynolds numbers ($760\text{-}10^4$), on the other hand, center-line radial velocity does not decrease continuously along radial distance. Instead at r/R=1.32 (8mm away from impeller blade tip) it makes a local maxima. This effect is a result of the small size of eddies which are generated by the interaction between the impeller and baffle and they contain significant portion of the total kinetic energy. Moreover, the differences between location of the radial and tangential velocity components can be used to estimate the average eddy size roughly in this region. When the radial velocity is measured at r/R=2, the effect of eddies disappears and as expected radial velocity decreases. This trend goes on until Re<300 which correspond to the transition region.

Below that value or in laminar region the effect of the eddies completely disappears as expected (see Figure 5.1.1.2)

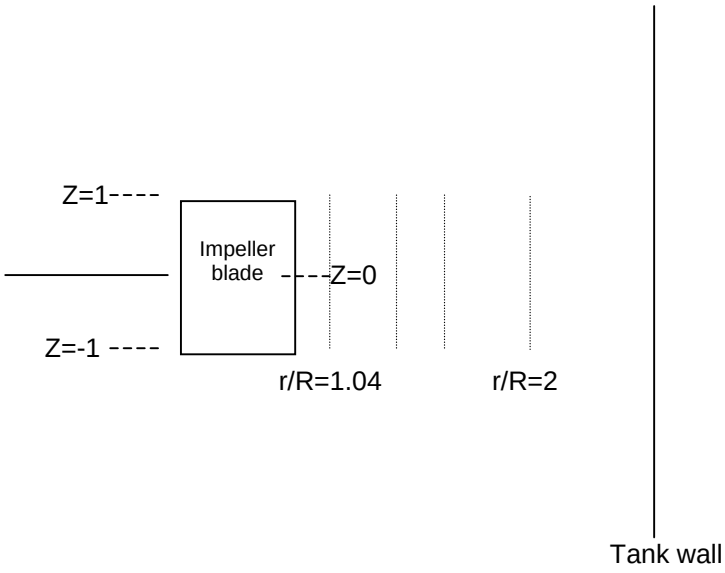

Figure 5.1.1.1. The observation points in the radial direction from the impeller blade to tank wall.

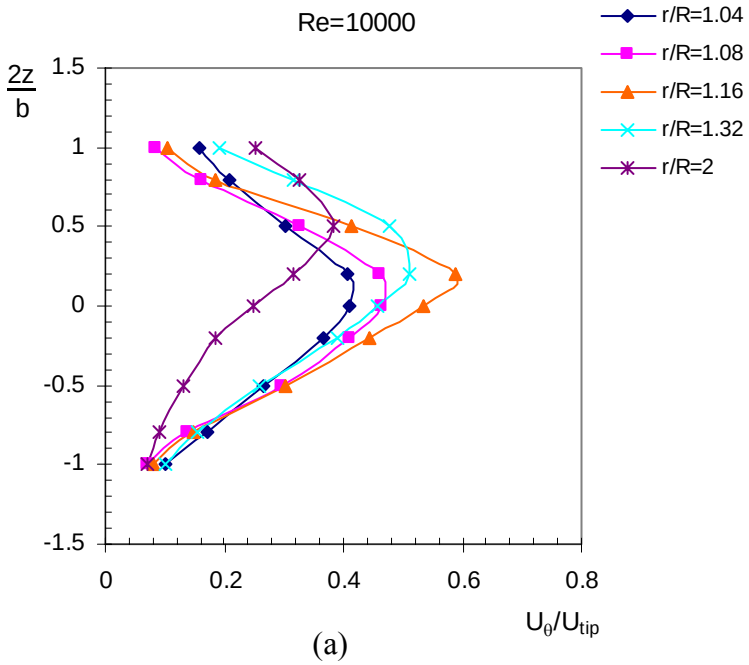

(a)

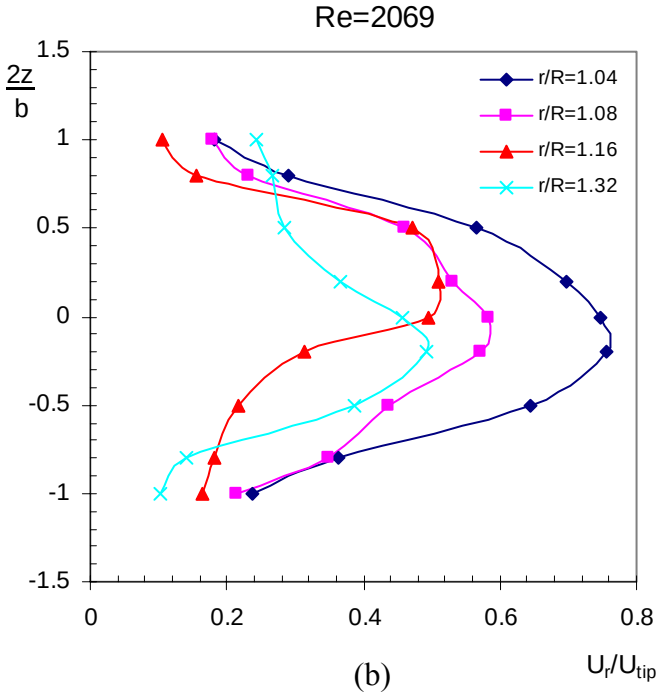

(b)

Figure 5.1.1.2. Axial distribution of the radial velocity profiles at various normalized radial positions at different Reynolds numbers: (a) Re=10000, (b) Re=2069, (c) Re=760, (d) Re=100, (e) Re=20

Re:760

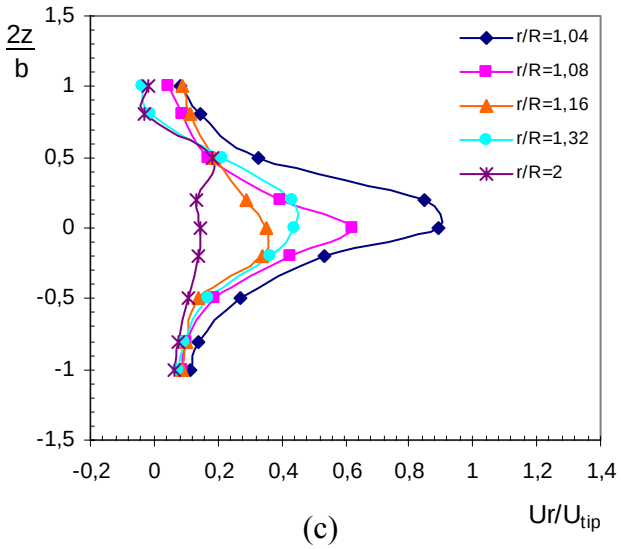

(c)

Re:100

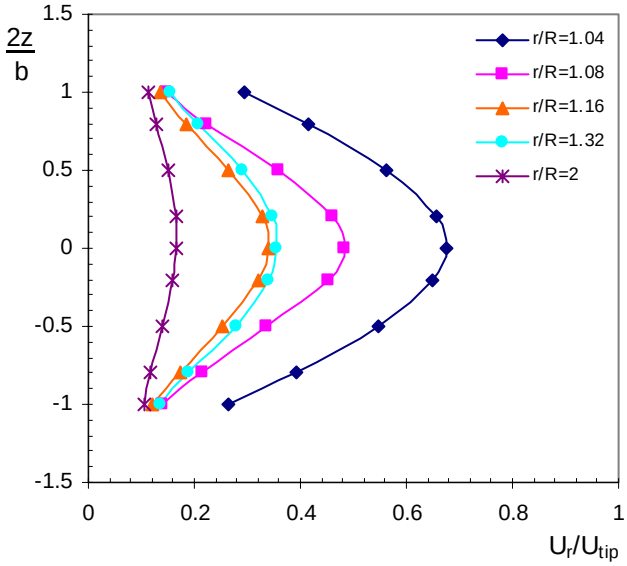

(d)

Figure 5.1.1.2. (continued)

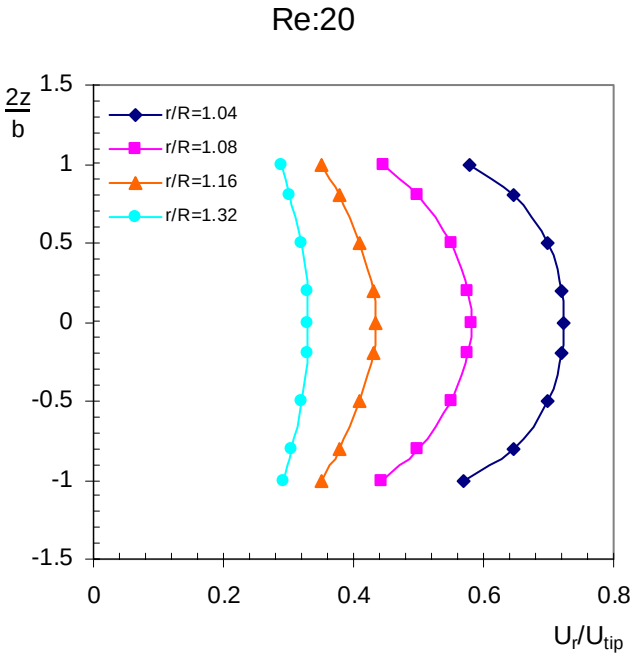

(e)

Figure 5.1.1.2. (continued)

5.1.2. Tangential flow pattern

Tangential velocities at different Reynolds numbers and at various radial positions are presented in Figure 5.1.2.1. Their magnitudes are higher compared to the radial components. Also, they are almost symmetrical with respect to the impeller axis and to the plane of impeller rotation. Tangential velocity components increase near the impeller but away from the impeller decrease because of the baffles and the vortices, which are more pronounced as Re increases. Near the baffle region tangential velocities diminish for all Reynolds number as expected.

In the range where Reynolds number is larger than 100, maximum tangential velocity appears at the radial distance r/R=1.16 while maximum radial velocity appears at r/R=1.04. This may be due to vortex formation which changes the velocity

direction and as a result of this radial velocity is relatively small in the radial distance of r/R=1.16 where tangential velocity is maximum.

Table 5.1.2.1 shows the maximum value of predicted tangential velocities and corresponding maximum radial velocities at different Reynolds number. In this table (Re=2069) tangential velocity can exceed the tip speed due to acceleration of the fluid over the blades (Stoots and Richard, 1995). The prediction of the maximum tangential velocity accurately is crucial. Under prediction of the tangential velocity leads to subsequent under prediction of the radial velocity. The prediction both maximum tangential and radial velocities agree well with those reported in the literature (Ranade, 1997).

Table 5.1.2.1. Predicted maximum tangential and radial velocities

	Re=10000	Re=2069	Re=760	Re=100	Re=20
U_θ	0.842Utip	1.032Utip	0.760Utip	0.526Utip	0.220Utip
U_r	0.600Utip	0.870Utip	0.622Utip	0.481Utip	0.580Utip

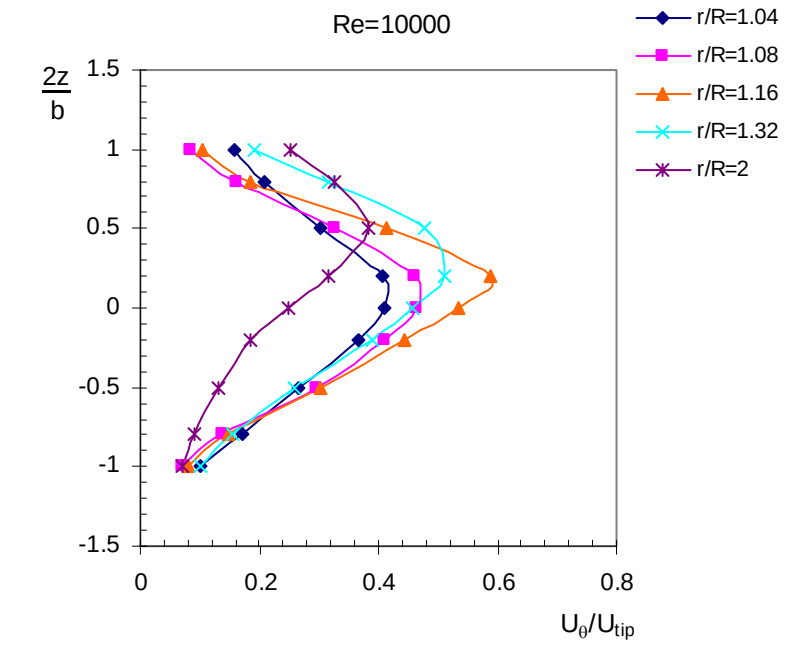

(a)

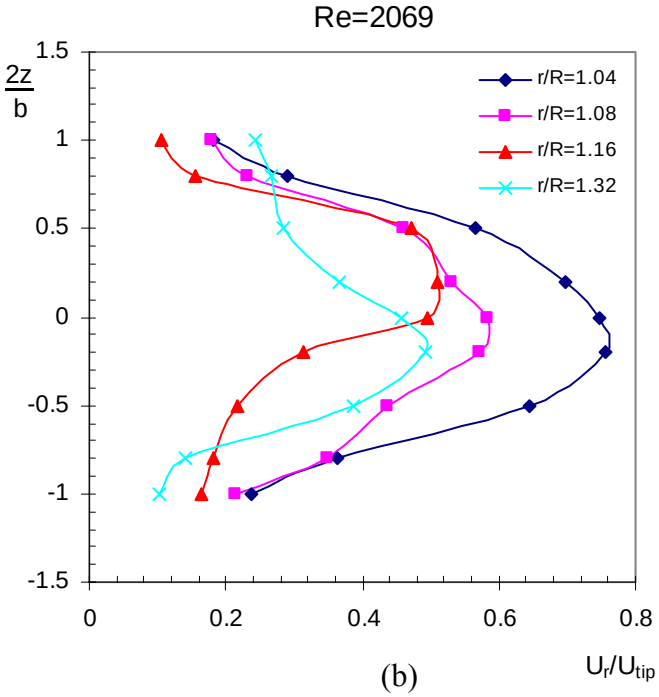

(b)

Figure 5.1.2.1. Axial distribution of the tangential velocity profiles at various normalized radial positions and various Reynolds numbers: (a) Re=10000, (b) Re=2069, (c) Re=760, (d) Re=100, (e) Re=20

Re=760

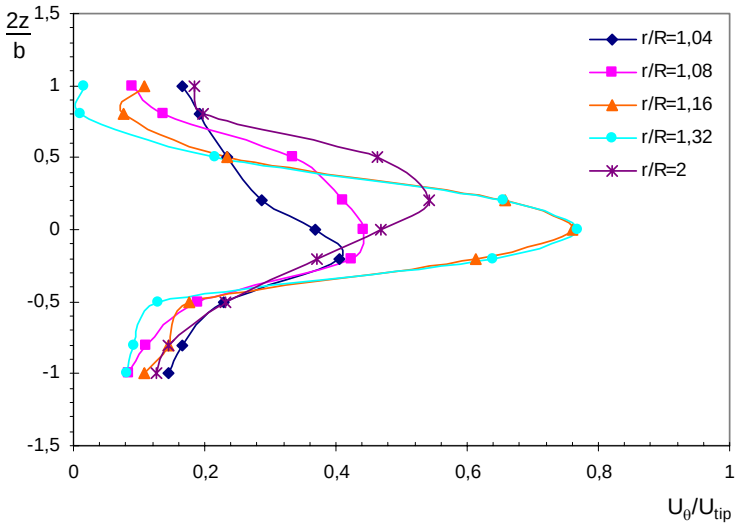

(c)

Re=100

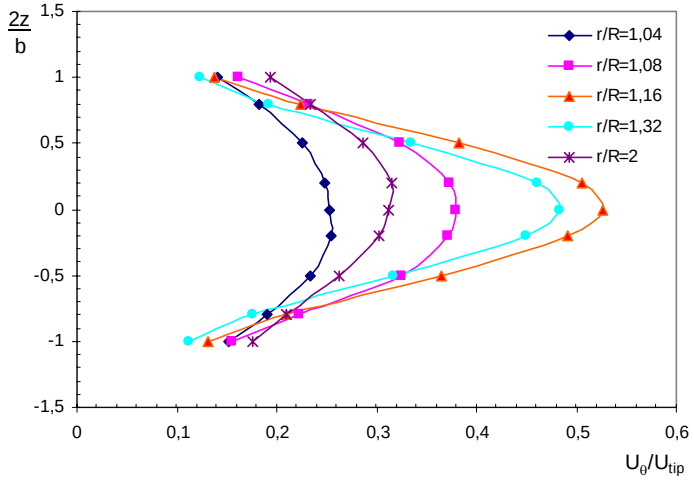

(d)

Figure 5.1.2.1. (continued)

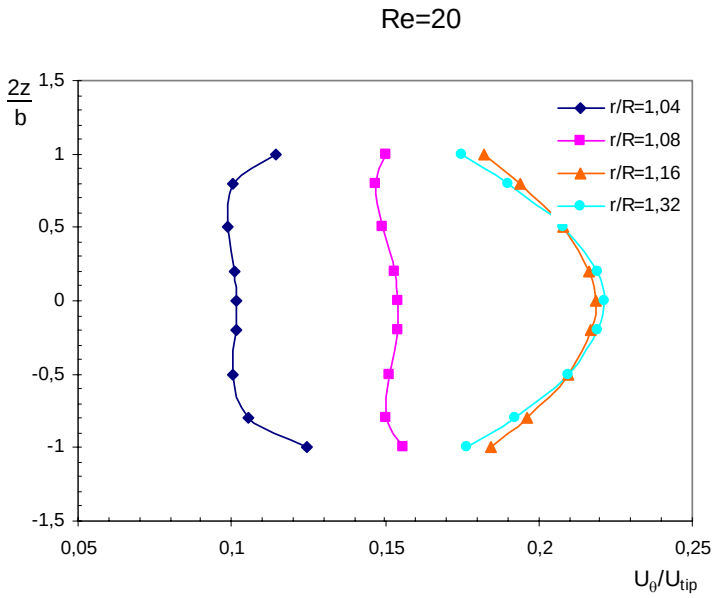

(e)

Figure 5.1.2.1. (continued)

5.1.3. Axial flow pattern

Axial velocities at different Reynolds numbers and at various radial positions are demonstrated in Figure 5.1.3.1. Axial velocities are much smaller than the other components through the impeller stream. In the range of Re>100 axial velocities fluctuate between negative and positive direction and this trend disappear at radial distance r/R=2. That is far away from the impeller they almost vanish. This may be the place where the impeller stream is about to split in to two streams, one flowing upward, the other flowing downward in to the bulk of the tank (see Figure 5.1.1).As shown in Figure 5.1.3.1-d-e at laminar region axial velocity components even near the impeller disappear. At this region radial and tangential velocity components are dominant.

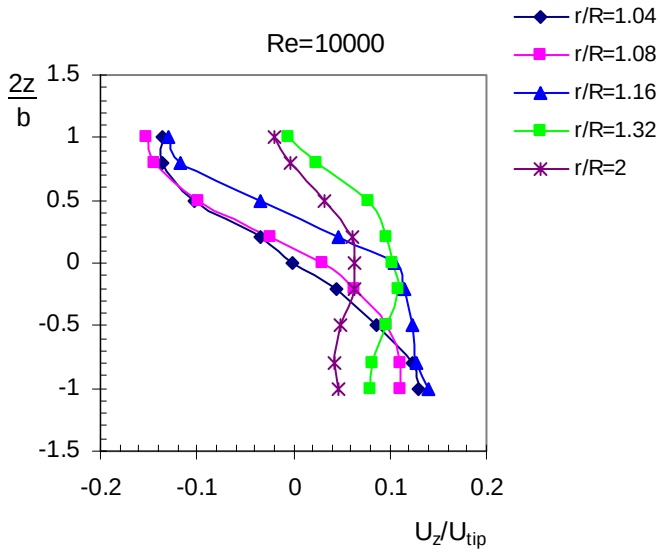

(a)

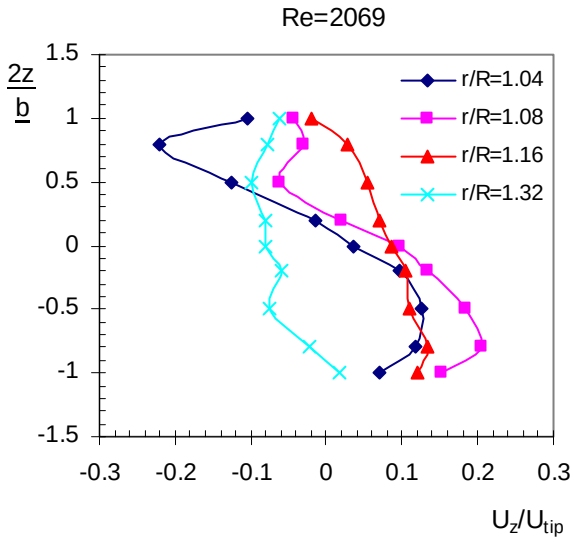

(b)

Figure 5.1.3.1. Axial distribution of the axial velocity profiles as a fuction of normalized radial positions at different Reynolds numbers: (a)Re=10000, (b) Re=2069, (c) Re=760, (d) Re=100, (e) Re=20

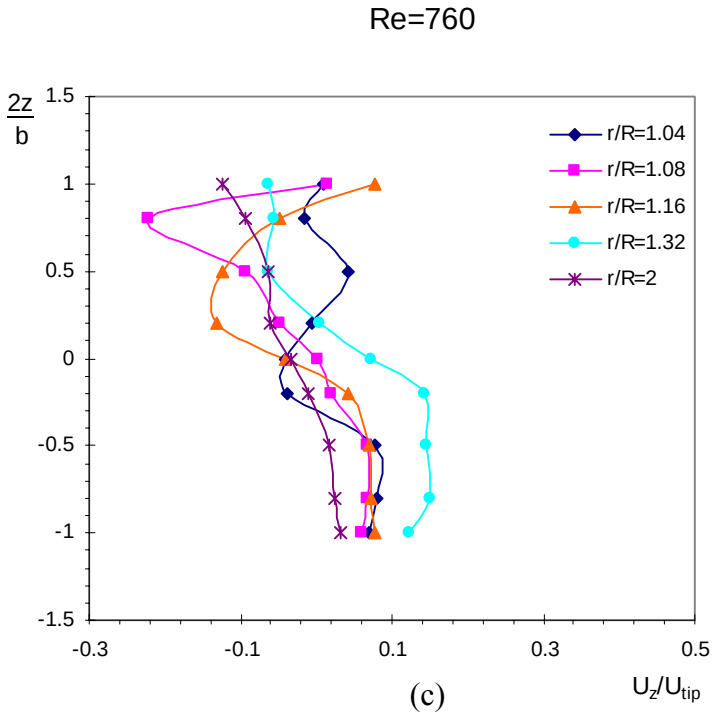

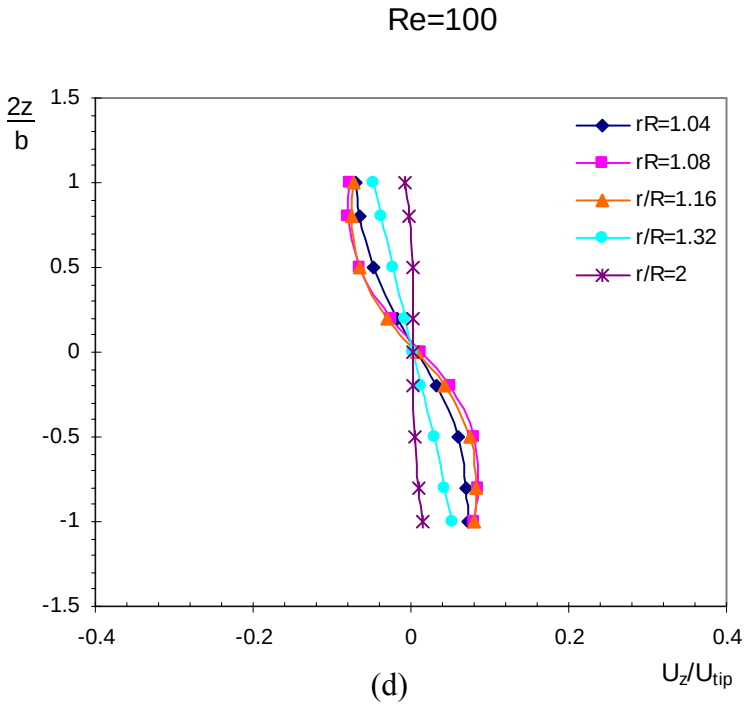

Figure 5.1.3.1. (continued)

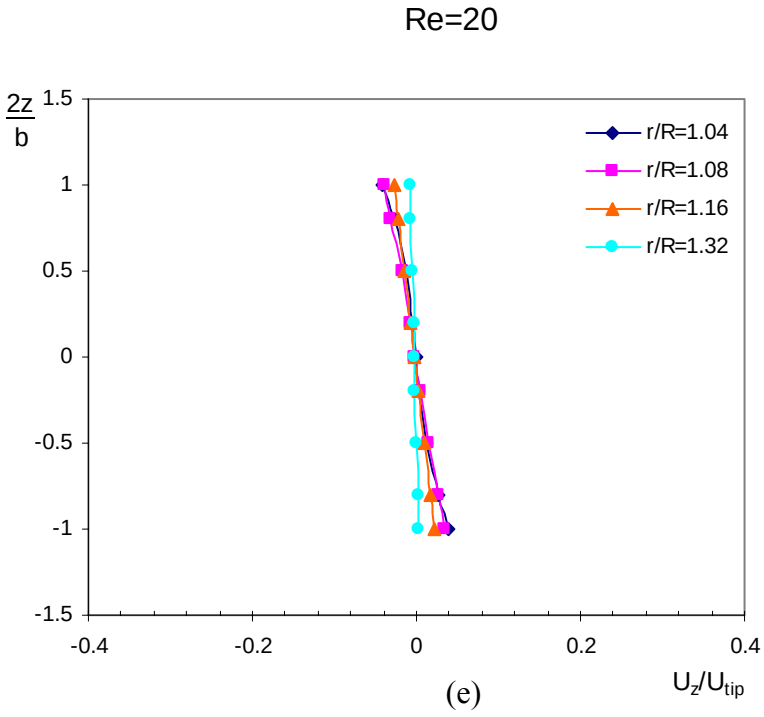

Figure 5.1.3.1. (continued)

5.1.4. Flow field at different axial location

The radial, tangential and axial velocity components at different axial locations in the tank were calculated. They are the axial location of the impeller blade (z=0), 25 mm above and 35 mm below the impeller as shown Figure 5.1.4.1.

Impeller plane velocity profiles:

Radial, tangential and axial velocity components at z=0 are depicted in Figure 5.1.4.2-4. In these figures horizontal axis represents the radial position, which is normalized by the impeller radius and vertical axis shows the velocities normalized by the impeller tip velocity.

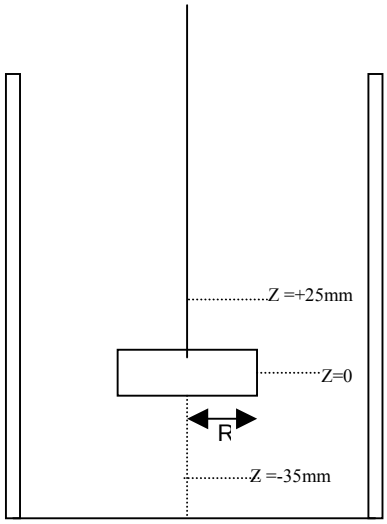

Figure 5.1.4.1. Axial positions of the tank cross-sections in which velocity components are presented.

Impeller plane radial velocity:

Figure 5.1.4.2 shows the impeller plane radial velocity profiles at different Reynolds number. They are not significantly affected by the Reynolds number that is in agreement with the previous work on Rushton turbines (Dyster at al., 1993). Also it is evident that the dimensionless radial velocity decreases at all Reynolds number with the increase in the radial distance. At low Reynolds number this trend is almost linear. Especially at high angular velocities $Re=10^4$ dimensionless radial velocity component near the baffles (r/R=2.3) increases. This is because the radial discharge of fluid flowing from the rotating impeller is disturbed by the baffles and causing relative increase in the fluids turbulence. But away from the baffle dimensionless radial velocity becoming again decreases.

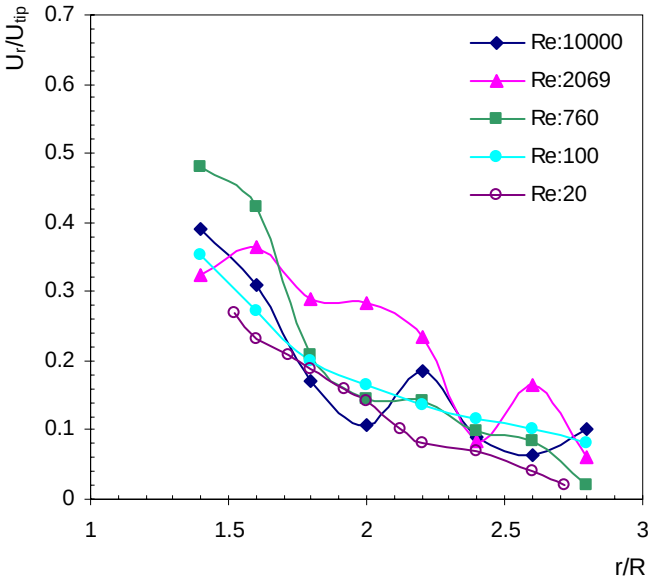

Figure 5.1.4.2 Radial velocity as a function of radial position and Re at z=0.

Impeller plane tangential velocity:

Figure 5.1.4.3 shows the center-line tangential velocity profiles at different Reynolds numbers. Dimensionless tangential velocity is appreciably decreases with increase the radial distance from the impeller. This is as a result of the baffle. Baffles eliminate the large scale vortex formation and induce turbulence.

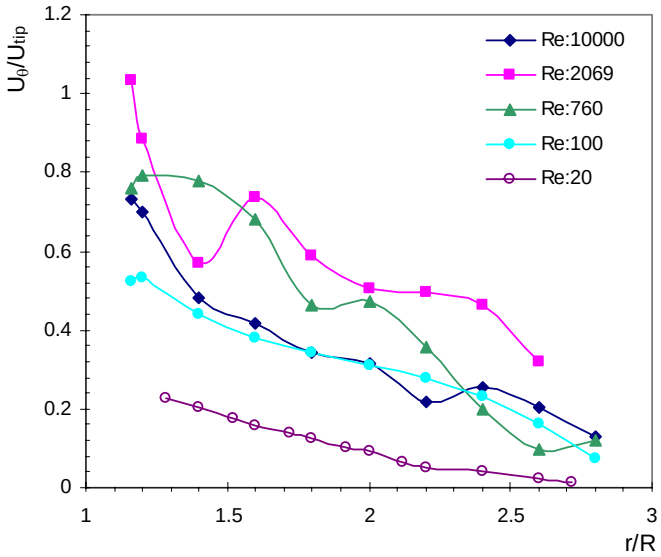

Figure 5.1.4.3 Tangential velocity as a function of radial position and Re at z=0

Impeller plane axial velocity:

Figure 5.1.4.4 shows the center-line axial velocity profiles with different Reynolds numbers. At low Reynolds numbers (Re=20, 100) dimensionless axial velocity is nearly zero within the radial position range, indicating that fluid in the laminar flow region either in the radial or tangential directions smoothly until the tank wall. However at high Reynolds numbers, turbulence onsets and axial velocity components fluctuate as other velocity components. This is expected because Rushton turbine dominantly generates radial flow pattern.

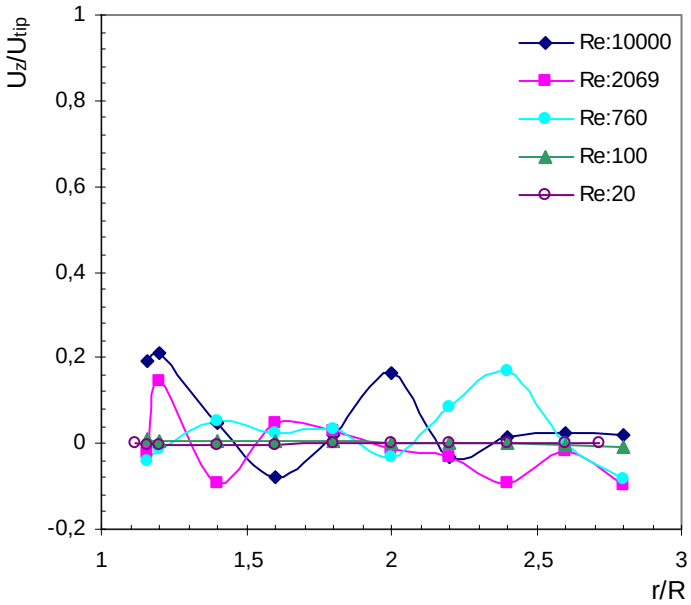

Figure 5.1.4.4 Axial velocity as a function of radial position and Re at z=0.

The flow pattern above the impeller:

Figure 5.1.4.5 shows the dimensionless radial, axial and tangential velocity patterns which have been calculated 25 mm above the center impeller plane at different radial positions and at different Reynolds numbers (20-10^4). In this figure at low Reynolds number radial velocity pattern above the impeller almost goes to zero, because of the stagnation region. Due to low angular speeds involved, the fluid at various locations of the tank remains stagnant. But at high Reynolds numbers radial velocity components decrease by making oscillation with the increasing radial position, whereas axial velocity profiles slowly increases with the increasing radial distance. This pattern in the axial flow can also be observed in the Figure 5.1.1 in which large scale smooth circulations occur at low Re and as radial position increases the movement of the fluid becomes rather in the axial direction. Similarly at high Re, fluid near the tank wall moves in the axial direction. But in this case this region is more confined to the regions that are much closer to the wall as opposed to

the low Re cases. Tangential velocities at high Reynolds number increases until a certain radial position (r/R=1.4) and then start to decrease towards zero. At low Reynolds numbers, along the radial distance there is not any variation of tangential velocity components.

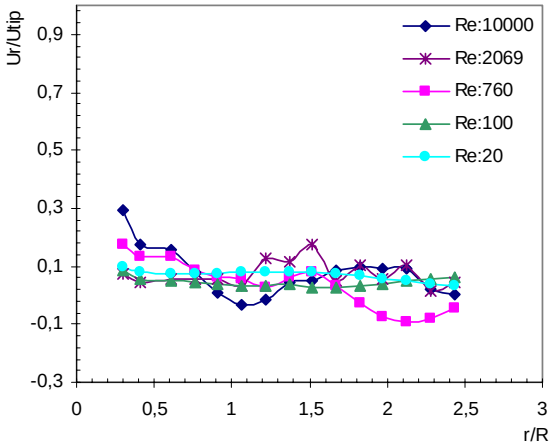

(a)

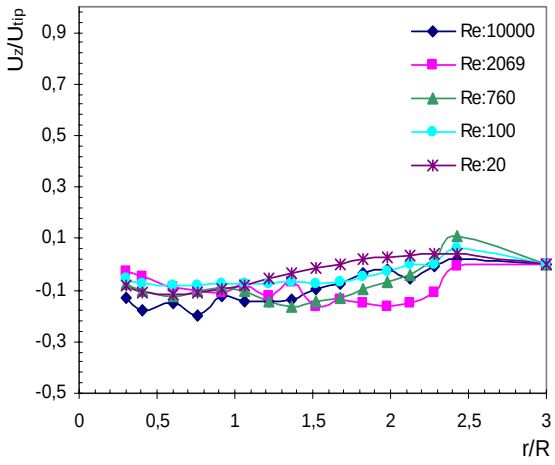

(b)

Figure 5.1.4.5. Velocity components as a function of radial position and Re above the impeller (z=+25 mm) (a) radial velocity, (b) axial velocity, (c) tangential velocity.

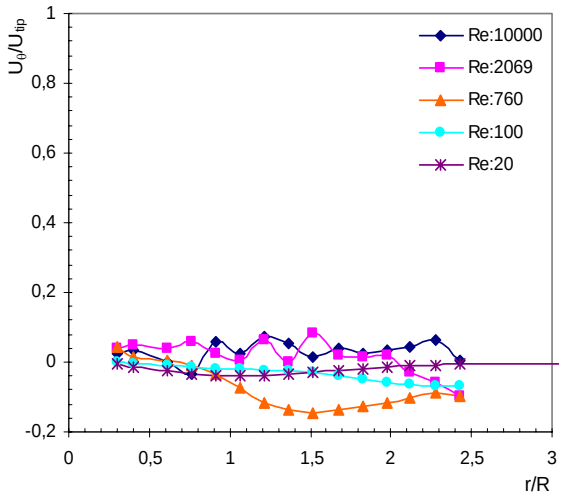

(c)

Figure 5.1.4.5. (continued)

The flow pattern below impeller blade:

Figure 5.1.4.6 shows the dimensionless radial, axial and tangential velocity patterns as a function of radial position and Re. In this figure radial velocity at high Reynolds numbers decreases along radial distance. However there is not any significant change in radial velocity below the impeller at low Reynolds numbers. Axial velocity at low Reynolds numbers almost goes to the zero along the radial distance. Actually flow pattern in the axial direction is quite similar to the above impeller cross-section. The main differences are the negative or downward direction of the velocity and more pronounced oscillations due to the presence of the tank bottom. However as Re gets higher decrease below to zero with increase the radial position. Tangential velocity at low Reynolds numbers does not change along the radial distance but with increase the Reynolds numbers they goes to zero along the radial position.

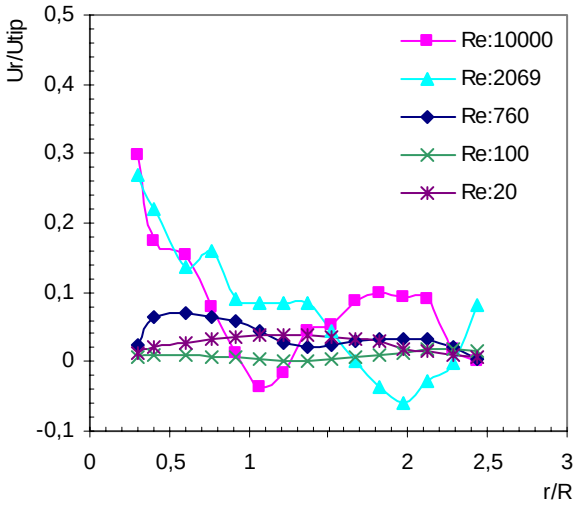

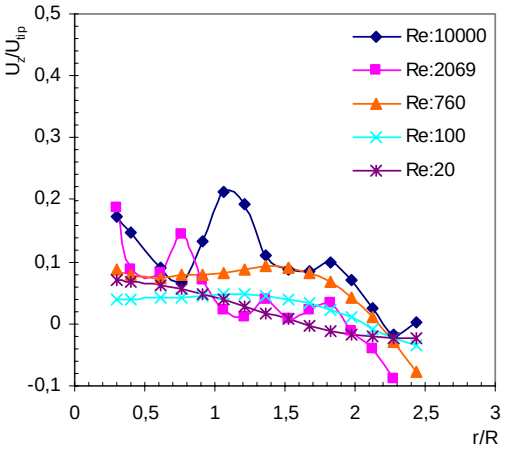

(b)

Figure 5.1.4.6 Velocity components as a function of radial position and Re below the impeller (z=-35 mm) (a) radial velocity, (b) axial velocity, (c) tangential velocity.

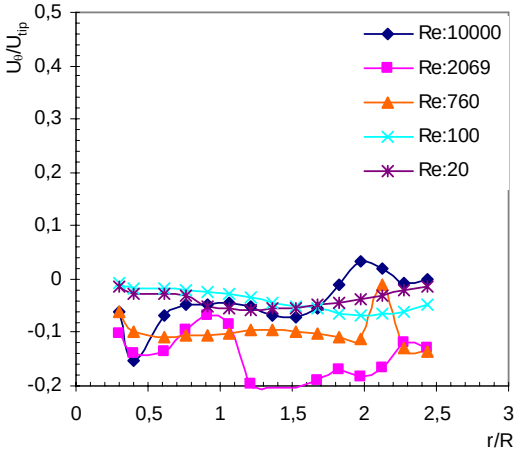

(c)

Figure 5.1.4.6. (continued)

5.1.5 The effects of the baffle presence on the flow field

The effects of the baffles on the radial and tangential velocity profiles are investigated at Re=760. Figure 5.1.5.1 shows the axial profile radial velocity components at radial distance 8mm from the impeller edge with baffle and without baffles. It can be seen that at the same radial distance, the radial velocity with baffles is greater than that without baffles. This is because of the baffles reduce the vortex as a result of this radial velocity decreases while tangential velocity components increases at the same radial distance as shown Figure 5.1.5.2.

Tangential velocity greatly decreases by insertion of baffles. In unbaffled stirred tank tangential velocity proportional to the vortex zone radius and it increase the increasing impeller speed. Therefore in unbaffled system tangential velocity increased with increasing impeller speed while radial velocity decreased.

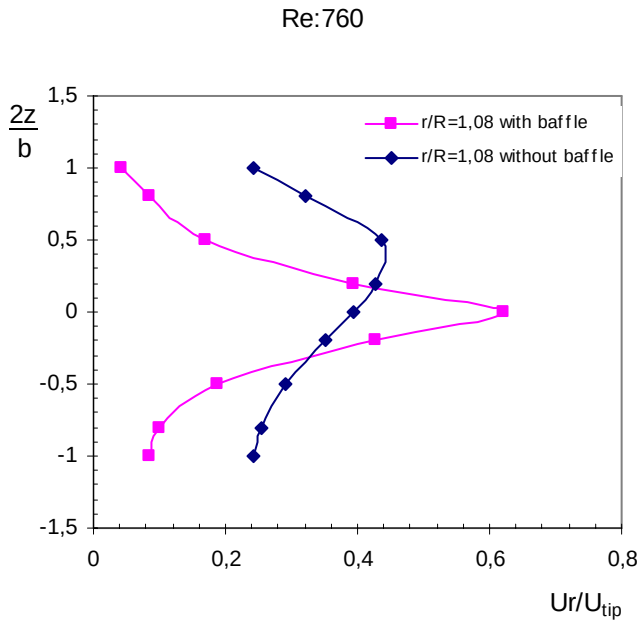

Figure 5.1.5.1 Axial profile radial velocity at Re=760

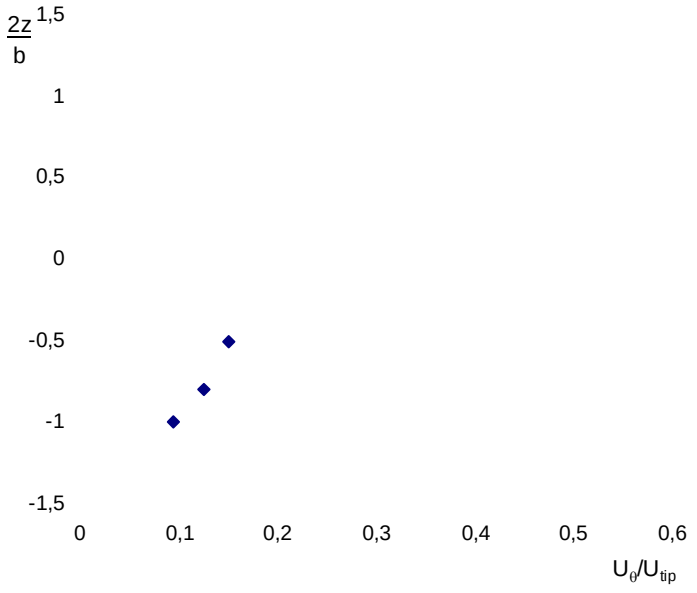

Figure 5.1.5.2 Axial profile tangential velocity at Re=760

5.1.6 Kinetic energy and kinetic energy dissipation rate

Turbulent kinetic energy and turbulent dissipation rate are evaluated at Reynold number 10^4 using k-ε model. The value of k calculated from equation (5.1.6.1):

$$k = \frac{1}{2}(\overline{V_r^2} + \overline{V_\theta^2} + \overline{V_z^2}) \qquad (5.1.6.1)$$

where $\overline{V_r^2}$,$\overline{V_\theta^2}$, $\overline{V_z^2}$ are the fluctuating velocities radial, tangential and axial direction respectively. Figure 5.1.6.1 depicts the turbulent kinetic energy, which is normalized by U^2_{tip} at the various radial locations from the blade edge. Near the impeller change in the k values as a function of axial locations occur stronger than those regions of more distant regions. Higher turbulent kinetic energies in vicinity of the impeller can be expected. The fluctuations in the k values with respect to axial position indicate that there are regions where fluid has a higher kinetic energy than others which can be explained through the turbulent eddies having characteristic length and velocity scales of the impeller height and velocity, respectively.

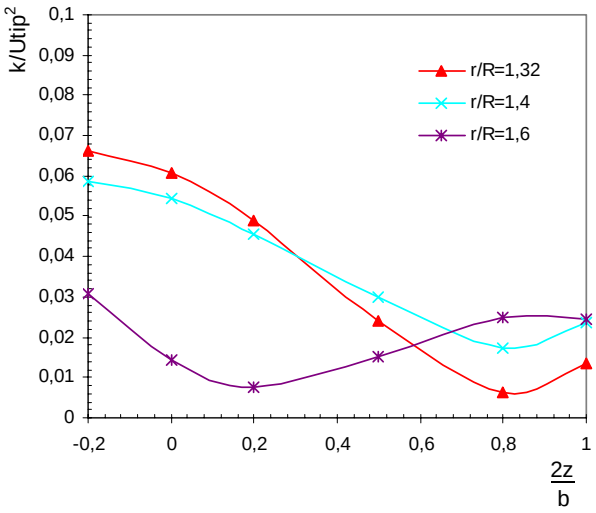

Figure 5.1.6.1 Axial distribution of the turbulent kinetic energy distribution at various radial locations.

Turbulent dissipation rate:

Turbulent dissipation rate can be defined as:

$$\varepsilon = \frac{Ak^{3/2}}{L}$$

where A is the constant, determined experimentally and it is approximately unity. L is the geometrical distance commonly chosen as impeller blade height (b) (Calabrese and et al., 1989). The characteristic features of turbulence irregularity and disorderliness, involve various periodicities and scales. For this reason turbulence consists of eddies of ever-smaller size. All these various sized eddies have a certain kinetic energy, determined by the intensity of the velocity fluctuation (Hinze, 1975). In the stirred tank small size eddies are generated by the impeller baffle interaction and they contain significant portion of the total kinetic energy. Turbulent energy is mostly dissipated by viscous effects in these smaller eddies. Figure 5.1.6.2 shows the radial profiles of the turbulent dissipation rate normalized with the tank average power consumption rate through impeller. Maximum dissipation rates occur

approximately at the mid point of the impeller stream where fraction of the small size eddies is high.

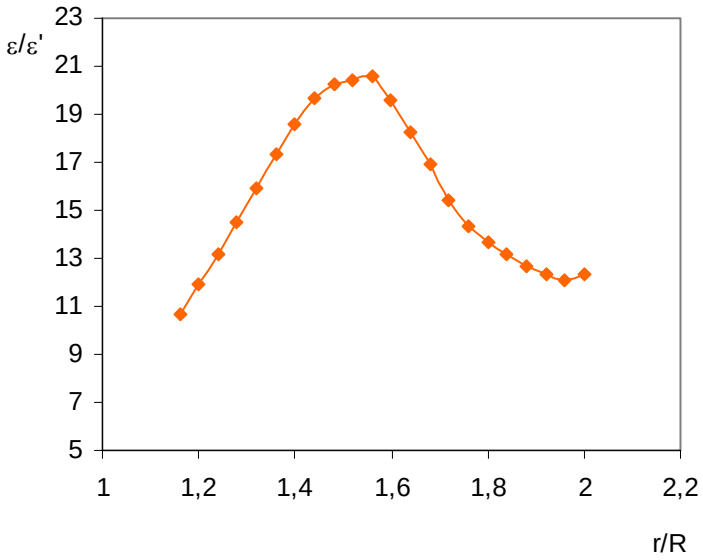

Figure 5.1.6.2 Radial distribution of the turbulent kinetic energy dissipation rate.

5.2 Power Number

Second part of our study is on the determination of the power consumption and the effects of the baffle length on the power number at different Reynolds numbers. Several shape factors have strong effect on the power number which are given in Chapter 2. In this section only one of those parameters, baffle length, is considered since it has been reported as the most effective parameter on the power consumption among the shape factors in the literature (Holland and Chapman, 1996).

Figure 5.2.1 shows the experimentally obtained power number versus Re, which is plotted in log-log scale for a standard tank configuration. Figure 5.2.1 shows that at low Reynolds numbers the plot is linear. In this range the viscous forces dominate the system. As the Reynolds number increases the flow changes from laminar to turbulent, the power curve becomes horizontal. For lower impeller

Reynolds numbers (10 and 760), the predicted power numbers are in excellent agreement with the reported data (Bates et al., 1963). For the turbulent regime, the power number is rather under predicted (approximately 28 %). This can be due the constant parameter used in k-epsilon model, which may not be accurate enough for the flow field in stirred tanks.

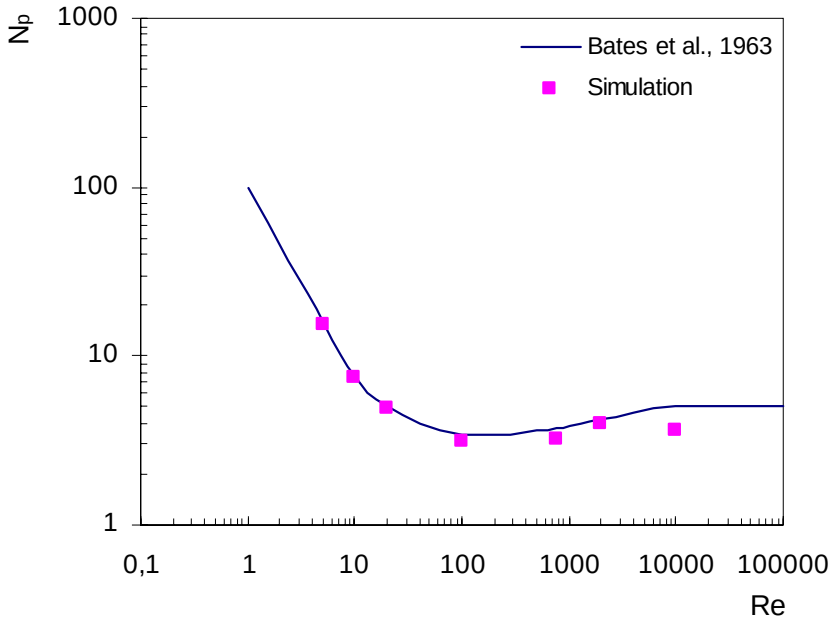

Effect of the baffle length on power number:

Figure 5.2.2 shows the effect of the baffle length on the power number. In this figure horizontal axis depicts baffle length normalized with the impeller diameter. At both Re=760 and Re=10, power number gets higher with increasing w/D_i ratio. This is because of the larger baffle area which in turn leads to increased turbulent kinetic energy dissipation rate near the baffle surfaces.

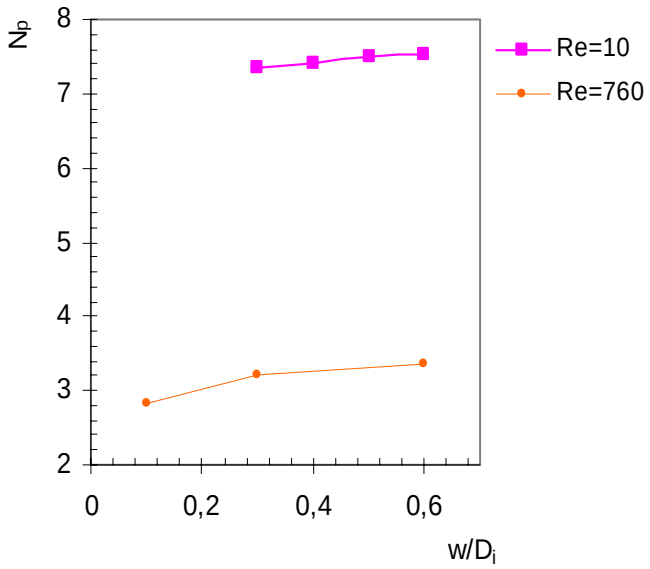

Figure 5.2.2. Effect of the baffle length on the power number

CHAPTER 6

CONCLUSIONS

The flow field and power consumption generated by Ruhton turbine impeller have been calculated using computational fluid dynamics techniques in conjuction with a multiple frame of reference method for various Reynolds numbers in both laminar and turbulent regime. The results obtained in this study allow one to draw the following conclusions:

1. Multiple frame of reference method has demonstrated that it is able to simulate the flow in stirred tanks and to produce realistic predictions.
2. In the r-z plane a strong radially oriented flow is observed to emerge from the impeller, producing two main recirculation flows, one above and the other below the impeller plane. Location of the circulation loops' centers change with increasing Reynolds numbers and move closer to the impeller plane.
3. Axial distribution of the center-line radial velocity components decrease with increasing radial distance from the impeller. But tangential velocity remain higher than the radial velocity and increase until radial distance r/R=1.16. After this location decreases with increasing radial distance. The axial velocity component is much smaller than the other components through the impeller stream and far away from the impeller it almost vanishes.

4. Impeller plane radial velocity is not significantly affected by the Reynolds numbers. Tangential velocity appreciable decrease at higher radial positions or away from the impeller region for all Re numbers. Axial velocity is found nearly zero especially in the laminar region.
5. At low Re numbers, radial velocity above the impeller becomes almost zero because of the stagnation region. However Tangential velocity is found to increase until a certain radial position (r/R=1.4) and then starts to decrease towards zero. Axial velocity diminishes along the radial position.
6. Radial velocity decreases below the impeller along the radial distance but tangential velocity does not change. Axial velocity exhibits similar characteristics to the axial velocity above the impeller.
7. Radial velocity component in an unbaffled vessel significantly decreases while tangential velocity gets higher at the same radial position.
8. Turbulent kinetic energy decreases as a function of radial position at Re=10000. In addition, maximum turbulent kinetic energy dissipation rate is found approximately at the mid point of the impeller stream where fraction of the small sized eddies is higher compared to the other tank locations.
9. Power curve is found in excellent agreement with the experimental data. Using larger baffle lengths lead to higher power consumption or power number.

REFERENCES

Abbott, Michael B., 1989, "Computational fluid dynamics: an introduction for engineers", Longman Scientific & Technical New York.

Bakker A., K. J. Mysers, R.W. Ward and C.K. Lee, 1996, "The Laminar and Turbulence Flow Pattern of Pitched Blade Turbine", Trans. I. Chem. E. 74, pp. 485-491.

Bakker, A. and Van den Akker, H. E. A., 1992, "A computational study on dispersing gas in stirred reactor, in Fluid Mechanics of Mixing", Kluwer Academic Publishers.

Bakker, A., R.D. Laroche, M.H. Wang and R.V. Calabrese, 1997, "Sliding Mesh Simulation of Laminar Flow in Stirred Reactors", Trans. Inst. Chem. Eng. 75, pp. 42-44.

Bates, R.L., Fondy, P.L., and Corpstein, R.R., 1963, "An examination of some geometrical parameters of impeller power", Ind. Eng. Chem. Proc. Des. Dev., 2: 310.

C. Hirsch, 1997, "Numerical Computation of Internal and External Flows", John Wiley & Sons.

Brucato, A., Ciofalo, M., Grisafi, F. and Micale, G., 1998, "Numerical prediction of flow fields in baffled stirred vessels: A comparison of alternative modeling approaches", Chem.Engng Sci., 53, pp. 3653-3684.

Calabrese, R. and Stoots, C. M., 1989, “Flow in the impeller region of a stirred tank”, Chem. Eng. Prog., pp.43-50.

D.H. Norrie and G. de Vries, 1978, “An Introduction to Finite Element Analysis”, Academic press New York.

DeSouza, A. ande Brezina, V., 1972, “Fluid Dynamics and Flow Patterns in Stirred Tanks with a Turbine Impeller”, Can.J. Chem. Engng., 50, pp. 15-23.

Dyster, K. N., Koutsakos, E., Jaworski, Z. and Nienow, A.E., 1993, “An LDA study of the radial discharge velocities generated by a Rushton turbine”, Chem. Engng Res. Des., 71, 11.

Fluent, 2000, “Journal articles by Fluent software users”, Fluent.

Harvey, P.S. and Greaves, M., 1982, “Turbulent flow in agitated vessel”, Trans. IChemE., 60, pp. 195-210.

Holland, F. A., Chapman, F.S., 1966, “Liquid Mixing and Processing in Stirred Tanks”, Lever Brothers Company, New York.

J. N. Reddy, 1993, “An Introduction to the Finite element Method”, McGraw-Hill.
J. O. Hinze, 1975, “Turbulence”, McGraw-Hill.

Jaworski, Z., Nienow, A.W., Koutsakos, E., Dyster, K., 1996, “An LDA Study of Turbulent Flow in a Baffled Vessel Agitated by an Axial, Down-pumping Hydrofil Impeller”, Can. J. Chem. Eng., 74, pp. 3-15.

Joel H. Ferziger and M. Peric, 1996, “Computational Methods for Fluid Dynamics”, Springer-Verlag.

Kresta, S.M. and P.E. Wood, 1991, “Prediction of Three Dimensional Turbulence Flow in Stirred Tanks”, AIChE., 37, pp. 448-460.

Kresta, S.M. and P.E. Wood, 1993,”The Flow Field Produced by a Pitched Blade Turbine: Characterization of the Turbulence and Estimation of Dissipation Rate”, Chem. Eng. Sci., 48, pp. 1761-1773.

Lee, K. C., Ng, K. and Yanneskis, M., 1996, “Sliding mesh predictions of turbulent flow around Rushton impellers”, IChemE Symp. Ser. 140, 47-58.

M. Griebel, T. Dornseifer and T. Neunhoeffer, 1998, “Numerical Simulation in Fluid Dynamics”, SIAM.

Nagata, S., 1975, “Mixing Principle and Applications”, Wiley New York.

Naude, I., Xuereb, C. and Bertrand, J., 1998, “Direct Prediction of the Flows Induced by Propeller in an Agitated Vessel Using an Unstructured Mesh”, Can. J. Chem. Eng., 76, pp. 631-640.

Periclous, K.A. and Patel, M. K., 1987, “The modeling of tangential and axial agitators in chemical reactors”, PhysicoChem. Hydrodyn., 8, pp. 105-123.

Placek, J., Tavlarides, L. L., Smith, G. W. and Fort, I., 1986, “Turbulent flow in stirred tanks”, AIChE, 32, 1771.

Ranade, V.V. and Dommeti, S.M.S., 1996, “Computational Snapshot of flow Generated by Axial Impellers in Baffled Stirred Vessel”, Trans. IChemE., 74, A, pp. 476-484.

Ranade, V.V. and Joshi, J.B., 1990b, “Flow generated by a Disc Turbine: Part II Mathematical Modeling and Comparison with Experimental Data”, Trans.IhemE., 68, A, pp. 34-50.

Ranade, V.V. Joshi, J.B. and Marathe, A.G., 1989, “Flow generated by pitched blade turbines II: simulation using k-epsilon model”, Chem. Engng. Comm., 81, pp. 225-248.

Ranade, V.V., 1997, “An efficient computational model for simulating flow in stirred vessels: a case of Rushton turbine”, Chem.Engng Sci., 52, pp. 4473-4484.

Ranade, V.V.and Joshi, J.B., 1990a, “Flow generated by a Disc Turbine: Part I Experimental”, Trans.IchemE., 68, A, pp. 19-33.

Roache, Patrick J., 1976, “Computational Fluid Dynamics”, Hermose.

Sahu, A.K., Kumar, P., Patwardhan, A.W., Joshi, J.B., 1999, “CFD modeling and mixing in stirred tanks”, Chem.Engng Sci., 54, pp. 2285-2293.

Stoots, C. M. and Calabrese, R.V., 1995, “Mean velocity field relative to a Rushton turbine blade”, A.I.Ch.E. J., 41, 1.

Tatterson, G.B., 1994, “Scaleup and Design of Industrial Mixing Process”, McGraw-Hill, New York.

Versteeg, H. K. and Malalaseke, W., 1995, “An introduction to computational Fluid Dynamics: The finite volume method”, Addison-Wesley.

Wu, H., G.K. Patterson and M. Van Doorn, 1989, “Distribution of Turbulent Flow Parameters in a Stirred Mixer”, Chem. Eng. Sci., 44, pp. 2207-2221.

Xu, Y. and McGrath, G., 1986, “Computational Fluid Dynamics Predictions of Stirred Tank Flows”, Trans. IChemE., 74, pp.471-475.